HHS Public Access

Author manuscript

Nat Cancer. Author manuscript; available in PMC 2021 November 26.

Published in final edited form as:

Nat Cancer. 2020 October ; 1(10): 1010–1024. doi:10.1038/s43018-020-00116-1.

FoxM1 insufficiency hyperactivates Ect2-RhoA-mDia1 signaling to drive cancer

Jazeel F. Limzerwala[1], **Karthik B. Jeganathan**[2], **Jake A. Kloeber**[1,3], **Brian A. Davies**[1], **Cheng Zhang**[4], **Ines Sturmlechner**[2], **Jian Zhong**[2], **Raul Fierro Velasco**[2], **Alan P. Fields**[5], **Yaxia Yuan**[6], **Darren J. Baker**[1,2], **Daohong Zhou**[6], **Hu Li**[4], **David J. Katzmann**[1], **Jan M. van Deursen**[1,2,*]

[1]Department of Biochemistry and Molecular Biology, Mayo Clinic Rochester, MN, USA

[2]Department of Pediatric and Adolescent Medicine, Mayo Clinic Rochester, MN, USA

[3]Department of Mayo Clinic Medical Scientist Training Program, Mayo Clinic Rochester, MN, USA

[4]Department of Molecular Pharmacology and Experimental Therapeutics, Mayo Clinic Rochester, MN, USA

[5]Department of Cancer Biology, Mayo Clinic, Jacksonville, FL, USA

[6]Department of Pharmacodynamics, University of Florida, Gainesville, FL, USA

Abstract

FoxM1 activates genes that regulate S-G2-M cell-cycle progression and, when overexpressed, is associated with poor clinical outcome in multiple cancers. Here we identify FoxM1 as a tumor suppressor in mice that, through its N-terminal domain, binds to and inhibits Ect2 to limit the activity of RhoA GTPase and its effector mDia1, a catalyst of cortical actin nucleation. FoxM1 insufficiency impedes centrosome movement through excessive cortical actin polymerization, thereby causing the formation of non-perpendicular mitotic spindles that missegregate chromosomes and drive tumorigenesis in mice. Importantly, low *FOXM1* expression correlates with RhoA GTPase hyperactivity in multiple human cancer types, indicating that suppression of the newly discovered Ect2-RhoAmDia1 oncogenic axis by FoxM1 is clinically relevant. Furthermore, by dissecting the domain requirements through which FoxM1 inhibits Ect2 GEF activity, we provide mechanistic insight for the development of pharmacological approaches that target protumorigenic RhoA activity.

Rho GTPases are conserved molecular switches that act as signal transducers in complex biological networks that control fundamental cellular processes such as cytoskeleton organization, cell migration, proliferation, survival and apoptosis, all of which are

* **Correspondence:** vandeursen.jan@mayo.edu .

Author contributions: J.F.L. and J.M.v.D. designed experiments, interpreted data, and wrote the manuscript with input from all authors. I.S., C.Z. and H.L. performed RNA sequencing and systems biology analyses. J.A.K. performed experiments pertaining to ROCK-Myosin signaling with J.F.L. B.A.D. and D.J.K. assisted with recombinant protein production and conducted *in vitro* binding experiments in collaboration with J.F.L. K.B.J. performed biochemical experiments, and R.F.V. immunofluorescence and histological assessments on mouse tissues with J.F.L. A.P.F. Y.Y. and D.Z. collaborated with J.F.L. on FoxM1-Ect2 binding studies. D.J.B. assisted with data interpretation and statistical analyses. J.M.v.D. supervised and directed all aspects of the study.

Competing interests: None.

deregulated in human cancers[1–4]. Rho GTPases are active in the GTP-bound state, enabling interaction with downstream effector proteins that mediate context-dependent responses to external signaling cues. Rho GTPase activity is tightly regulated by a multitude of guanine nucleotide-exchange factors (GEFs) that catalyze the GTP-bound state, GTPase activating proteins (GAPs) that stimulate GTP hydrolysis, and guanine dissociation inhibitors (GDIs) that bind Rho GTPases in the GDP-bound state to prevent both GTP exchange and relocation to subcellular locations where Rho GTPases are active[1]. Post-translational modifications contribute to the spatio-temporal control of Rho GTPases, including prenylation, phosphorylation and ubiquitination[5]. Perturbations in the intricate signaling networks that lead to overactivation of Rho GTPases have been linked to neoplastic cell growth[6–11]. Particularly overactivation of GEFs appears to be a prominent source of uncontrolled Rho GTPase activity in human malignancies[12].

One of these GEFs, Ect2, activates RhoA, Rac1 and Cdc42, and as such plays a central role in processes such as cell division and mitotic cell rounding, invasion, proliferation and DNA damage repair[13,14]. *ECT2* is overexpressed in various human malignancies, including ovarian, esophageal and non-small cell lung cancer (NSCLC), often through amplification of the chromosome 3q26 locus[13,15,16]. Ect2 mainly resides in the nucleus, where it is autoinhibited when N-terminal tandem BRCT domains interact with the C-terminal DH-PH domain that confers GEF activity[14,17]. Phosphorylation of multiple Ect2 residues by Cdk1 and atypical PKCι relieve this autoinhibition and allow the protein to relocate to its sites of action[14,18]. Nuclear-to-cytoplasmic relocation and activation of RhoA are Ect2 properties critical for transformation of cultured fibroblasts[19], while neoplastic growth of human *KRAS-p53*-driven lung adenocarcinoma cells requires Ect2 GEF activity towards Rac1, with activated Rac1 engaging NPM and UBF1 to promote rDNA transcription[20]. However, the full spectrum of effector molecules, and biological processes that act downstream of Ect2 to drive neoplastic transformation are incompletely understood. Furthermore, how Ect2 activity is deregulated to drive cancer beyond 3q26 amplification remains largely unknown.

Forkhead family member FoxM1 is a proto-oncogenic transcription factor that regulates cell division by activating the expression of genes implicated in the G_1/S and G_2/M phase transitions and mitotic progression and whose overexpression tightly correlates with poor clinical outcome in many human cancer types [21–24]. Here we show that FoxM1 inhibits Ect2 through a non-transcriptional mechanism and that Ect2 hyperactivation caused by FoxM1 insufficiency engages a previously unrecognized oncogenic pathway involving RhoA-mDia1-mediated cortical actin hyperpolymerization that drives tumor development by causing chromosomal instability (CIN).

RESULTS

FoxM1 is a haplo-insufficient tumor suppressor

Analysis of data from The Cancer Genome Atlas (TCGA) indicated that loss of *FOXM1* gene copy number occurs in multiple human cancers, raising the possibility that FoxM1 might have tumor suppressive functions in addition to its role as a proto-oncogene (Extended Data Fig. 1a). *Foxm1* null mice die between day E13.5-E18.5[25], precluding the use of a classical gene knockout strategy to test this possibility. To bypass this problem, we

engineered mutant mice that express low amounts of FoxM1 by using a *Foxm1* knockout (*Foxm1*$^{-}$) allele in combination with either a hypomorphic (*Foxm1*^{H}) or a wildtype (*Foxm1*$^{+}$) allele (Extended Data Fig. 1b). The resulting *Foxm1*$^{+/-}$ and *Foxm1*$^{-/H}$ mice were postnatally viable and indistinguishable from wildtype littermates. Western blotting of *Foxm1*$^{+/-}$ and *Foxm1*$^{-/H}$ MEFs revealed FoxM1 reductions of ~68% and ~77%, respectively (Fig. 1a and Fig. Extended Data Fig. 1c). Substantial reductions were also observed in lung, liver, spleen, and colon (Fig. 1a and Extended Data Fig. 1c, d). Reduced FoxM1 expression in MEFs altered transcription of 10 out of 11 established FoxM1 target genes, 7 of which showed a further decline in *Foxm1*$^{-/-}$ MEFs (Fig. 1b). Although *Foxm1*$^{+/-}$ and *Foxm1*$^{-/H}$ mice exhibited no overt signs of ill health by 16 months of age, inspection of internal organs revealed that both strains were prone to tumors, including lung and liver tumors and lymphomas (Fig. 1c,d). Western blot analysis revealed that lymphomas from *Foxm1*$^{+/-}$ and *Foxm1*$^{-/H}$ mice still had ample FoxM1 protein, implying that loss of heterozygosity of *Foxm1* is not a requirement for tumor formation (Fig. 1e). Furthermore, loss of a single *Foxm1*allele increased lung tumor multiplicity in the *Kras*^{LA1} model for lung tumorigenesis (Fig. 1f). In humans, low *FOXM1* expression in colorectal tumors is associated with poor clinical outcome (Extended Data Fig. 1e), which prompted us to test whether *Foxm1* haploinsufficiency promotes intestinal tumorigenesis in the *Apc*$^{+/Min}$ model. Indeed, the incidence and multiplicity of both small intestinal and colonic lesions were increased in *Foxm1*$^{+/-}$;*Apc*$^{+/Min}$ mice compared to *Apc*$^{+/Min}$ littermates (Fig. 1g,h). Together these data identify *Foxm1* as a haplo-insufficient tumor suppressor.

To assess whether the observed tumor predisposition might be attributed to alterations in gene expression, we sequenced RNA extracted from *Foxm1*$^{+/+}$ and *Foxm1*$^{+/-}$ lung tissue when animals were 10 days old, an age when FoxM1 is transcriptionally active and lesions are lacking. Only one gene was found to be differentially expressed (Supplementary Table 1), implying that *Foxm1* insufficiency predisposes mice to tumors via a non-transcriptional mechanism.

FoxM1 deficiency causes slow centrosome movement and chromosome missegregation

To examine whether the tumor phenotypes of *Foxm1*$^{+/-}$ and *Foxm1*$^{-/H}$ mice might be caused by CIN, we performed chromosome counts on metaphase spreads of splenocytes from 5-month-old mice. We found that 16% of splenocytes of *Foxm1*$^{+/-}$ and 19% of *Foxm1*$^{-/H}$ mice were aneuploid, compared to only 2% of control splenocytes (Fig. 2a). Similar results were observed in MEFs, where *Foxm1*$^{+/+}$, *Foxm1*$^{+/-}$ and *Foxm1*$^{-/H}$ showed aneuploidy rates of 13%, 25% and 30%, respectively (Fig. 2b). Aneuploidy rates in *Foxm1*$^{-/-}$ MEFs were only slightly higher at 33%. Live-cell imaging of primary MEFs expressing H2B-mRFP revealed that all three mutants had higher rates of lagging chromosomes than wildtype MEFs, with *Foxm1*$^{-/-}$ MEFs also showing more chromosome misalignments (Fig. 2c).

Merotelic microtubule-kinetochore malattachments, the source of lagging chromosomes, can result from a multitude of mitotic defects, including defective attachment-error correction, aberrant mitotic timing, pseudo-bipolar or multipolar spindles[26], and spindles where the centrosomes are oriented non-perpendicularly to the metaphase plate (hereafter

non-perpendicular spindles)[27–29]. Strikingly, *Foxm1* mutants consistently had high rates of non-perpendicular spindles but no other defects causing lagging chromosomes (Fig. 2d and Extended Data Fig. 2a-c). Live-cell imaging of MEFs expressing H2B-YFP and γTubulin-tdTomato fusion proteins confirmed that non-perpendicular spindles were indeed the source of lagging chromosomes in FoxM1-insufficient MEFs (Fig. 2e).

Next, we screened *Foxm1* mutant MEFs for irregularities in centrosome disjunction and centrosome movement, both of which are known to cause non-perpendicular spindles[27–29]. While centrosome disjunction was unperturbed (Extended Data Fig. 2d), once separated, duplicated centrosomes moved to opposite poles with markedly reduced speed (Fig. 2f,g and Extended Data Fig. 2e). Eg5, the microtubule kinesin that drives centrosome movement, accumulated normally at centrosomes late in G_2, indicating that FoxM1 controls centrosome movement in an Eg5-independent manner (Extended Data Fig. 3a). Importantly, non-perpendicular spindles, and lagging and misaligned chromosomes were all observed at increased rates in hepatocytes of FoxM1-insufficient two days after partial hepatectomy (Fig. 2h-j), indicating that mitotic defects observed in MEFs occur also *in vivo*.

FoxM1 controls centrosome movement via a transcription-independent mechanism

To determine how FoxM1 controls the speed with which duplicated centrosomes move to opposite poles, we stably expressed tdTomato-tagged FoxM1 mutant mouse cDNA constructs in *Foxm1*$^{-/-}$ and *Foxm1*$^{-/H}$ MEFs and screened for correction of slow centrosome movement (Extended Data Fig. 3b). While ectopic expression of full-length FoxM1$^{1–757}$ restored proper movement, truncation mutant FoxM1$^{232–757}$ with increased transcriptional activity[30,31]did not (Fig. 3a and Extended Data Fig. 3c). In contrast, the complementary deletion mutant consisting of the N-terminal domain (NTD), FoxM1$^{1–232}$, restored proper centrosome movement. In addition, rates of non-perpendicular spindles, chromosome missegregation, and aneuploidization were concomitantly corrected (Fig. 3b-d and Extended Data Fig. 3d,e). Ectopic expression of FoxM1$^{1–232}$ failed to normalize FoxM1 target gene expression in *Foxm1*$^{+/-}$ and *Foxm1*$^{-/-}$ MEFs, as demonstrated by RNA sequencing (Fig. 3e and Supplementary Table 2). FoxM1$^{1–232}$ also had no impact on altering FoxM1 target gene expression or mitotic fidelity when ectopically expressed in *Foxm1*$^{+/+}$ MEFs, indicating that it does not act in a dominant-negative manner transcriptionally (Fig. 3e and Extended Data Fig. 3f). Chromosome missegregation in *Foxm1*$^{-/-}$ MEFs has been linked to delayed G_2/M progression resulting from *Foxm1* target gene deregulation[21]. However, while flow cytometry analyses of asynchronously growing MEFs stained for propidium iodide confirmed that G_2/M progression is delayed in *Foxm1*$^{-/-}$ MEFs, *Foxm1*$^{+/-}$ and *Foxm1*$^{-/H}$ MEFs showed no such delay (Extended Data Fig. 3g,h). Furthermore, ectopic FoxM1$^{1–232}$ expression in *Foxm1*$^{-/-}$ MEFs, failed to normalize G_2/M progression (Extended Data Fig. 3g,h). Collectively, the above data indicate that FoxM1 facilitates proper chromosome segregation via a non-transcriptional mechanism.

FoxM1 restrains cortical actin nucleation through its N-terminal domain

To identify how the FoxM1-NTD might control centrosome movement, we focused on the actomyosin cortex, an intricate plasma membrane-associated network comprised of actin filaments, myosin motors, and various actin-binding and modulating proteins[32] along which

astral microtubules emanating from centrosomes move in a myosin II-dependent fashion[33]. F-actin visualization by TRITC-phalloidin revealed that FoxM1-insufficient MEFs exhibit excessive cortical actin nucleation starting from G_1 and continuing until anaphase (Fig. 4a and Extended Data Fig. 4a,b). Despite increased cortical actin nucleation, FoxM1-insufficient MEFs retained normal cortical myosin levels as determined by immunolabeling of metaphase cells for myosin light chain 2 (MLC2) (Extended Data Fig. 4c). Normalization of cortical actin levels in these cells, by the actin depolymerizing drug Cytochalasin D or the pan-Formin inhibitor SMIFH2, restored proper centrosome movement and formation of perpendicular spindles (Fig. 4b and Extended Data Fig. 4d,e). Furthermore, SMIFH2 treatment of *Foxm1*$^{-/-}$ MEFs fully restored accurate chromosome segregation (Extended Data Fig. 4f). Collectively, these data indicate that excessive cortical actin nucleation causes the slow centrosome movement phenotype of FoxM1-insufficient cells and the consequent formation of error-prone non-perpendicular mitotic spindles.

Because SMIFH2 inhibits mDia1 (*Diaph1*), a RhoA-activated cortical actin nucleator responsible for cell rounding in mitosis and assembling the actomyosin contractile ring in cytokinesis[34–36], we speculated that the FoxM1-NTD might keep cortical actin nucleation in check by inhibiting RhoA-mDia1 signaling. Indeed, loss of FoxM1 markedly elevated cortical RhoA activity, as measured by the use of an established RhoA biosensor, anillin-GFP[37] (Fig. 4c). Ectopic expression of the FoxM1-NTD was sufficient to normalize RhoA activity in *Foxm1*$^{-/-}$ MEFs (Fig. 4c).

Furthermore, suppression of RhoA hyperactivity with C3 transferase (C3) or knockdown of *Diaph1* normalized cortical actin nucleation in *Foxm1*$^{-/-}$ MEFs, rescuing slow centrosome movement, non-perpendicular spindle formation, and chromosome missegregation (Fig. 4d-l). The same was also true for depletion of Ect2, the GEF that activates RhoA-mDia signaling(Fig. 4g-l), supporting the idea that FoxM1-NTD inhibits cortical actin nucleation by inhibiting Ect2-mediated RhoA-mDia1 signaling. RhoA also controls Rho-kinase (ROCK) activity, which prompted us to examine FoxM1-insufficient MEFs for hyperphosphorylation of key ROCK substrates, including MLC2 (at Ser19 and Thr18/Ser19), MYPT (at Thr696), and LIMK1/2 (at Thr508/Thr505) by western blot analysis. None of the substrates showed a significant increase in phosphorylation in *Foxm1*$^{+/-}$, *Foxm1*$^{-/H}$ and *Foxm1*$^{-/-}$ MEFs, although the biological variability for pMYPT^{Thr696} was rather high in *Foxm1*$^{-/H}$ and *Foxm1*$^{-/-}$ MEFs (Extended Data Fig. 4g,h). Furthermore, cortical pMLC2^{Ser19} levels appeared normal in FoxM1-insufficient MEFs (Extended Data Fig. 4i). Thus, FoxM1 insufficiency hyperactivates Ect2-RhoA-mDia1 signaling and seemingly leaves RhoA-ROCK-Myosin signaling unaffected.

Besides RhoA, Ect2 activates Rac1 and Cdc42[14], raising the possibility that these GTPases contribute to the observed mitotic phenotypes. However, unlike RhoA knockdown, Rac1 or Cdc42 knockdown in *Foxm1*$^{-/-}$ MEFs failed to rescue defects in cortical actin nucleation, centrosome movement, and spindle symmetry (Extended Data Fig. 5a-d). Consistent with this, Rac1 and Cdc42 activity as well as the phosphorylation status of two key substrates of the Rac1 and Cdc42 effector protein Pak1, Merlin^{Ser518} and Mek1/2$^{Ser217/221}$, seemed unaltered in *Foxm1*$^{-/-}$ MEFs (Extended Data Fig. 5e,f). Thus, Ect2 seems to selectively hyperactivate RhoA in FoxM1-insufficient cells.

FoxM1 binds Ect2 to inhibit RhoA GTPase activation

Immunoprecipitation experiments revealed that FoxM1 and Ect2 interact under physiological conditions in MEFs, primary human skin fibroblasts (HSF) and lung cancer cell lines (Fig. 5a and Extended Data Fig. 6a). Ect2 and FoxM1 were abundantly present in both nuclear and cytoplasmic cell fractions but only interacted with each other in the cytoplasm (Fig. 5b,c). The FoxM1-NTD exhibited the same distribution pattern as full-length FoxM1 and also exclusively interacted with Ect2 in the cytoplasmic compartment (Fig. 5b,c and Extended Data Fig. 6b,c). Recombinant FoxM1-NTD purified from bacteria inhibited Ect2-mediated activation of RhoA in an *in vitro* guanine nucleotide exchange assay (Fig. 5d) and ectopically expressed FoxM1-NTD restored proper cortical actin nucleation in *Foxm1*$^{-/-}$ MEFs (Extended Data Fig. 6d). Mapping experiments revealed that FoxM1-NTD binds to Ect2 via both the tandem BRCT domains (137–328) in the N-terminus as well as the C-domain (775–883) in the C-terminus (Fig. 5e-g). Intramolecular interactions between the BRCT domains and the C-domain mediate autoinhibition of Ect2[17]. Our finding that FoxM1 NTD can bind to both of these domains suggests NTD association inhibits Ect2 through promoting or stabilizing the autoinhibited conformation. Furthermore, our finding that FoxM1 and Ect2 directly interact implied that the relative levels of FoxM1 and Ect2 are critically important for proper cortical actin nucleation. To test this experimentally, we overexpressed HA-Ect2 in wildtype MEFs and stained the cells for TRITC-phalloidin. Indeed, Ect2 overexpression caused excessive cortical actin nucleation and recapitulated all other phenotypes associated with FoxM1 insufficiency (Extended Data Fig. 6e-j). These observations support the conclusion that FoxM1, via its NTD, binds to Ect2 in the cytoplasm to inhibit RhoAmDia1-mediated cortical actin hypernucleation, indicating that proper cortical actin levels are critical for normal chromosome segregation.

Excessive cortical actin density yields dysfunctional mitotic spindles

Depletion of *FOXM1* from primary HSFs phenocopied the mitotic defects observed in FoxM1-deficient MEFs, demonstrating conservation of FoxM1's role in limiting cortical actin nucleation (Extended Data Fig. 7a-e). To obtain independent evidence that perturbations in this process create error-prone non-perpendicular spindles, we increased cortical actin density in wildtype MEFs with the actin-polymerizing drug Jasplakinolide, depletion of the actin depolymerizing protein Cofilin1 (encoded by *Cfl1*), or knockdown of actin capping protein beta (CapZβ; encoded by *Capzb*)[38]. Indeed, all three interventions resulted in slow centrosome movement, formation of non-perpendicular spindles, and chromosome missegregation (Fig. 6a-j and Extended Data Fig. 7f-k). *Cfl1*$^{+/-}$ MEFs were similarly affected (Extended Data Fig. 7l-p). Jasplakinolide treatment also impeded centrosome movement in primary HSFs (Fig. 6k). Reduction of astral microtubule density with a low dose of nocodazole, restored centrosome movement in Jasplakinolide-treated or *Cfl1*-depleted wildtype MEFs (Fig. 6l). Likewise, low-dose nocodazole also corrected centrosome movement defects of FoxM1-insufficient MEFs (Fig. 6m).

These observations led us to speculate that excessive cortical actin nucleation creates an actomyosin cortex that is too rigid for astral microtubules to move at a rate necessary for perpendicular spindle formation. To test this idea, we relaxed the cortical network by suppressing myosin activity directly with Blebbistatin or indirectly through inhibition

of ROCK with Fasudil or Y-27632. Remarkably, all three treatments restored proper centrosome movement and mitotic spindle symmetry in FoxM1-insufficient MEFs (Fig. 6n,o). We confirmed that neither of these treatments impacted cortical actin hypernucleation, and that the ROCK inhibitors reduced phosphorylation of cortical MLC2^{Ser19} (Extended Data Fig. 7q). Furthermore, Y-27632 treatment also normalized centrosome movement in CapZβ-depleted MEFs, which exhibit excessive cortical actin levels due to aberrant actin capping rather than RhoA hyperactivity (Extended Data Fig. 7r). Thus, excessive cortical rigidity resulting from uncontrolled actin nucleation impairs astral microtubule-mediated movement of centrosomes along the cell cortex to promote the formation of asymmetrical mitotic spindles.

RhoA hyperactivity is a feature of human cancers expressing low FOXM1

Next, we determined whether suppression of the Ect2-RhoA-mDia1 oncogenic axis by FoxM1 is clinically relevant using RNA sequencing data available from TCGA. In response to RhoA-mediated actin polymerization, two transcriptional co-activators, MRTF-A and YAP, enter the nucleus for target gene expression[39–41]. Using a panel of genes controlled by MRTF-A or YAP, or both (Supplementary Table 4), we assessed whether low *FOXM1* expression correlates with RhoA hyperactivity in a wide variety of human cancer types. For each type of cancer, we stratified tumors based on *FOXM1* mRNA levels into *FOXM1* high (top 15%) and low groups (bottom 15%). Low *FOXM1* expression correlated with RhoA GTPase hyperactivity in multiple major human cancer types, including breast (BRCA), liver (LIHC), and lung (LUAD and LUSC) cancers, whereas the *FOXM1* high group did not (Fig. 7a). About half of the genes of the RhoA hyperactivity signature used were commonly upregulated among all these four cancer types in the *FOXM1* low group (Fig. 7b-d).

YAP is an effector of the Hippo signaling pathway whose activity is inhibited by LATS1/2-mediated Ser127 phosphorylation[42]. However, changes in cytoskeleton organization driven by actin polymerization into stress fibers and ECM remodeling can mediate YAP entry into the nucleus to drive gene expression in conjunction with TEAD, independent of Hippo signaling[43,44]. Analysis of the cancer proteome atlas (TCPA) revealed a negative correlation between FOXM1 protein levels and YAP^{Ser127} phosphorylation in BRCA, LIHC, LUAD and LUSC datasets (Fig. 7e,f), further supporting the idea that induction of YAP-controlled genes in the *FOXM1* low cancer groups is driven by RhoA-activated actin polymerization. Collectively, our findings indicate that *FOXM1* insufficiency drives pro-tumorigenic RhoA signaling in prevalent human cancers.

Normalizing cortical actin density by NTD overexpression suppresses tumorigenesis

To test whether the FoxM1-NTD can restore tumor suppression in FoxM1-insufficient mice, we generated transgenic mice that ubiquitously expresses HA-tagged NTD (NTD^T) under the control of the CAGS promoter and bred it onto a *Foxm1*$^{+/-}$ genetic background (Fig. 8a and Extended Data Fig. 8a). While NTD^T suppressed aneuploidy caused by *Foxm1* haploinsufficiency, it had no impact on aneuploidy rates in wildtype mice (Fig. 8b and Extended Data Fig. 8b). Furthermore, NTD^T normalized cortical actin levels and corrected non-perpendicular spindle formation and chromosome segregation errors in *Foxm1*$^{-/-}$ MEFs, as well as in *Foxm1*$^{+/-}$ hepatocytes after partial hepatectomy (Fig. 8c and Extended

Data Fig. 8c-f). Importantly, NTD^T counteracted tumor predisposition of *Foxm1*$^{+/-}$ mice treated with 7,12-Dimethylbenz[a]anthracene (DMBA; Fig. 8d). NTD^T also neutralized the increase in tumor burden caused by *Foxm1* haploinsufficiency in both the *Kras*^{LA1} lung tumor model and the *Apc*$^{+/Min}$ intestinal tumor model (Fig. 8e-g). Collectively, these data indicate that the NTD^T suppresses aneuploidy and tumorigenesis *in vivo*, thereby implicating aberrant chromosome segregation due to excessive cortical actin nucleation as a driver of tumorigenesis.

Next, we explored the therapeutic potential of the NTD in a cancer model characterized by RhoA hyperactivity on a wildtype *Foxm1* background. To this end, we employed the well-established MMTV-*PyVT* breast cancer model with lung metastasis and elevated RhoA activity[45,46]. The median time to onset of the first palpable lesion in MMTV-*PyVT* females was 62 days versus 65 days in MMTV-*PyVT* females carrying NTD^T (Fig. 8h). Weekly measurements of tumor size over a 6-week period after the first tumor was palpable revealed a significant reduction in tumor growth in the presence of NTD^T which correlated with reduced RhoA activity (Fig. 8i and Extended Data Fig. 8g). Assessment of tumor dissemination rates 6 weeks after the first lesion was palpable, revealed a marked reduction in the number of metastatic lesions in MMTV*PyVT*;NTD^T females (Fig. 8j). In probing the underlying mechanism for reduced lung metastases, we observed that both primary and metastatic MMTV-*PyVT* tumor cells formed non-perpendicular spindles at high rates, which corresponded with high rates of lagging chromosomes (Fig. 8k,l), both of which were remedied by the NTD^T. Furthermore, tumor cells carrying the NTD^T had lower cortical actin levels than those without it (Fig. 8m). *Ect2* knockdown or treatment with a RhoA inhibitor in MMTV-*PyVT* tumor cells, also reduced rates of non-perpendicular spindles, lagging chromosomes and cortical actin levels (Extended Data Fig. 8k-n), suggesting that the NTD^T exerts its therapeutic effects on tumor growth and metastasis in the MMTV-*PyVT* model by normalizing Ect2-RhoA-driven cortical actin nucleation and CIN. Collectively, our data indicate that the NTD can inhibit Ect2-RhoA-mDia1 oncogenic signaling regardless of FoxM1 status, and reveal the potential of therapeutic strategies designed to attenuate rather than aggravate CIN in tumor cells by modulating RhoA activity.

DISCUSSION

Here we report that FoxM1 binds to and inhibits Ect2 to suppress an oncogenic Ect2-RhoA-mDia1 signaling axis that drives CIN by impeding centrosome movement through excessive cortical actin polymerization, causing the formation of non-perpendicular mitotic spindles that missegregate chromosomes (Extended Data Fig. 9). We find that low *FOXM1* expression correlates with RhoA GTPase hyperactivity in multiple human cancers, suggesting that this newly discovered tumor suppressive mechanism is frequently defective and clinically relevant.

The cell cortex: a novel target for deregulation in tumorigenesis

Our discovery here of a gene defect that disrupts the cell cortex as being cancer-causing, raises the important question as to what extent the more than 100 distinct elements of the elaborate actomyosin network also promote neoplastic transformation when defective.

Important clues are provided by experiments in which we increased cortical actin density, independent of FoxM1 insufficiency, by depleting Cofilin or Capzβ in wildtype MEFs (Extended Data Fig. 9). In both instances, increased cortical actin density phenocopied FoxM1 insufficiency. Interestingly, reducing cortex rigidity by inhibiting ROCK-mediated activation of myosin corrected all mitotic defects of Capzβ-deficient cells. Inhibition of myosin activity, either directly or indirectly through ROCK inhibition, produced similar corrective effects in FoxM1-insufficient cells, where we found no evidence for hyperactive ROCK-myosin signaling. Collectively these findings support a model in which cortical actin hypernucleation yields a cortex that is too rigid for astral microtubules to move along efficiently enough to yield perpendicular mitotic spindles.

FoxM1 selectively controls one of the oncogenic axes defined by Ect2 overactivation

We find that both Ect2 and FoxM1 localize in the nucleus as well as the cytoplasm, but that their interaction exclusively occurs in the cytoplasm, indicating that distinct subpopulations of FoxM1 function in Ect2 inhibition and transcriptional activation of target genes. In dissecting how Ect2 is regulated by FoxM1, we uncovered that the FoxM1-NTD interacts with tandem BRCT and C-domain of Ect2 reminiscent of an auto-inhibited state established through intra-molecular interaction[17]. The ability of FoxM1-NTD to bind these regions suggest that FoxM1 either facilitates or mimics Ect2 auto-inhibition to control the cortical actin nucleation activation pathway. However, this regulatory mechanism may not be relevant during cytokinesis as NTD overexpression did not impact Ect2-RhoA-mDia1 mediated formation of the contractile ring that splits the cell in two during cytokinesis[47]. One possibility is that FoxM1 and MgcRacGAP, the subunit of the centralspindlin complex that recruits Ect2 to the midbody in cytokinesis and locally activates its GEF activity[36], regulate distinct pools of Ect2 at different locations and times of the cell cycle. Alternatively, MgcRacGAP may simply become a preferred binding partner of Ect2 in cytokinesis, thereby displacing FoxM1 from Ect2.FoxM1 also showed selectivity for the Ect2 pool that targets RhoA, as two other Ect2-controlled GTPases, Rac1 and Cdc42, did not become hyperactive when FoxM1 was lacking. A recently identified nuclear Ect2-Rac1 oncogenic circuit engages NPM and UBF1 to promote the development of *KRAS-p53*-driven lung adenocarcinomas by stimulating rDNA transcription[20]. Ect2 hyperactivity here depends on PKCi-mediated Ect2^{T328} phosphorylation, as further demonstrated by the observation that pharmacological inhibition of PKCi attenuates lung tumorigenesis[48]. Thus, our findings presented here not only provide evidence for the existence of multiple oncogenic axes defined by Ect2 overactivation, but also that distinct inhibitors will need to be developed to target these axes for therapeutic purposes.

Inhibition of CIN: a novel anti-cancer therapeutic concept

Current anti-cancer therapies exploiting CIN are designed to perturb mitosis so severely that cancer cells die or undergo cellular senescence. However, although mitosis-targeting therapies can be successful, full eradication of cancer cells, drug resistance and toxicity are major challenges of this class of anti-cancer strategies[49,50]. With CIN being a near universal feature of cancer and evidence mounting that CIN is a key driver of intra-tumor heterogeneity, tumor evolution, metastasis and treatment failure[51–56], there is a renewed effort to identify novel CIN-based cancer therapies. Our demonstration

that transgenic expression of the FoxM1-NTD suppresses tumorigenesis and metastasis in FoxM1-insufficient and MMTV-*PyVT* mice, provides a molecular framework for the concept of therapeutically inhibiting CIN to suppress intra-tumor heterogeneity and disease progression. By dissecting the domain requirements through which FoxM1 inhibits Ect2 GEF activity, we provide mechanistic insight for the development of pharmacological approaches that limit CIN in cancers in which RhoA hyperactivity is driven by Ect2.

METHODS

Mouse strains

All mice were housed in a pathogen-free barrier environment with *ad libitum* access to food and water, 12-hour light and dark cycles, temperature between 68–79°F and humidity between 30–70%. Protocols were approved by the Mayo Clinic Institutional Animal Care and Use Committee and were carried out in compliance with ethical guidelines for animal welfare. The *Foxm1* hypomorphic allele (H), containing a neomycin selection cassette in reverse orientation, was generated using standard gene targeting and embryonic stem cell technology. The neomycin cassette was removed to generate the knockout allele (–) by crossing the mice with *Hprt*-Cre transgenic mice. *Foxm1* mutant mice were maintained on a mixed 129Sv/E x C57BL/6 genetic background. Mice (male and female) in the spontaneous tumor susceptibility study were euthanized at 16 months and major organs were screened for presence of overt tumors. Tumors were collected and histopathology was performed using standard procedures. For generation of *pCAGS-Rosa26-HA-FoxM1*$^{1–232}$ transgenic mice (NTD^{T}), homology arms spanning 1 kb of the 5’ end and 4 kb of the 3’ end were used to target HA-FoxM1$^{1–232}$ cDNA into the *Rosa26* locus of zygotes (C57BL/6) using CRISPR/Cas9 mediated gene targeting. *Cfl1* heterozygous mice were generated by deleting exon 2 of the *Cfl1* gene using CRISPR/Cas9 mediated gene editing in C57BL/6 fertilized eggs. Founder mice were back-crossed for 2 generations on C57BL/6 background prior to experimental use. *Kras*^{LA1} and *Apc*$^{+/Min}$ mice used in experiments were maintained as heterozygotes on C57BL/6 background. Mice on the *Apc*$^{+/Min}$ background were sacrificed 90 days after birth and the small intestine and colon were flushed with PBS and collected for tumor analysis. Mice on the *Kras*^{LA1} background were sacrificed at 6 weeks after birth and lungs collected for tumor analysis. DMBA (7,12-Dimehylbenz[a]anthracene) treatment involved a single application of 50 μl of 0.5% DMBA in acetone to the dorsal surface of mice on postnatal day 4–5. Mice were sacrificed 4 months later and the lung and skin were analyzed for overt tumors. For experiments involving the MMTV-*PyVT* mouse strain, male MMTV-*PyVT* mice on an FVB background (Stock #002374; The Jackson Laboratory) were crossed to female FoxM1-NTD^{T} mice to obtain experimental mice. Only female mice obtained from these breedings were used for experimentation. From 5 weeks of age, mice were examined three times-a-week for presence of palpable mammary tumors. After the first mammary tumor was palpated, mice were sacrificed 6 weeks later and the lungs were examined under a dissection microscope for presence of lung metastases. At least 15 mice were used in each group per experiment.

Cell Culture

Primary mouse embryonic fibroblasts (MEF) cultures from mutant *Foxm1* and *Cfl1* mice were generated and cultured as previously described[57]. Primary HSF were obtained from the Mayo Clinic core facility. H1299 and A549 cells were a kind gift from Dr. Scott Kaufmann (Mayo Clinic). At least 3 independent MEF/HSF lines per genotype were used at passage 4/5 for all experiments. All primary cultures and cell lines were maintained in DMEM (Gibco; 11960044) supplemented with 2 mM L-glutamine, non-essential amino acids, 1 mM sodium pyruvate, 50 μg ml^{-1} gentamicin, 50 μM β-mercaptoethanol and 10% heat-inactivated fetal calf serum. Mitotic MEFs were prepared by mechanical shake-off after arresting them for 4 h with 5 μM STLC (164739; Sigma-Aldrich). For experiments involving lentiviral overexpression or knockdown of genes, cultures were infected twice with the viral particles (once every 24 h) and selected with 2 μg ml^{-1} puromycin (Ant-pr-1; Invivogen) or 10 μg ml^{-1} blasticidin (R21001; Thermo Scientific, for overexpression of HA-Ect2) for 48 h prior to using cells for the experiments.

For the generation of tumor derived epithelial cells, freshly isolated tumors were washed twice with PBS and mechanically disrupted with scalpels. Suspensions were subsequently digested with liberase (05401127001; Roche) in trypsin-EDTA solution for 20–30 min, filtered through 100 μM cell strainers and collected by centrifugation (300*g*, 5 min). Cells were resuspended in complete DMEM/F12 media containing 25 μg/ml hydrocortisone, 25 ng/ml EGF, 5 μg/ml insulin, 10 ng/ml cholera toxin and 5 μM Y-27632 ROCK inhibitor, and co-cultured with irradiated feeder cells (3T3-J2 strain). Once cells reached 80–90% confluency, they were washed 3 times to remove any residual ROCK inhibitor, trypsinized and seeded on to glass slides without feeder cells and ROCK inhibitor for immunofluorescence experiments. 3–5 independent tumor derived cell lines per genotype were used for experiments. 50–75 cells per line were analyzed for lagging chromosome incidence and 15–20 cells per line were analyzed for non-perpendicular spindle formation and cortical actin intensity measurements. For experiments involving the shRNA-mediated knockdown of Ect2 in tumor epithelial cells, passage 2 cells were infected twice with lentivirus particles. 48 h after infection, cells were seeded on to glass slides in media containing 1 μg ml^{-1} of puromycin for immunofluorescence analyses.

Monastrol Washout Assay

Asynchronously growing MEFs on glass slides were treated with 100 μM monastrol in complete DMEM medium for 60 min to induce syntelic attachments. After 60 min, 10 μM MG132 was added to the cells for another 60 min. Cells were washed 3 times with complete DMEM to remove any residual monastrol, and released into medium containing 10 μM MG132 for a further 90 min to allow correction of syntelic attachment-induced chromosome misalignments. The cells were fixed in PBS/4% PFA for 10 min, permeabilized with Triton-X 100 for 10 min and stained with Hoechst 33342 for 2 min. Cells were scored for presence of chromosome misalignments using a fluorescence microscope.

Plasmids and lentivirus production

ShRNA sequences were obtained from the RNAi consortium (TRC, Broad Institute) and cloned into pLKO.1 vector (Addgene #10878) according to their corresponding

protocol[58]. Please see Supplementary Table 3 for sequences used. The non-targeting TRC2 shRNA [referred to as scrambled shRNA (*shScr*), Sigma-Aldrich, SCH202] was used as a negative control. *Foxm1*cDNA was obtained from Origene (MC221366 corresponding to NM_008021) and the different deletion mutants were sub-cloned into pLVX-tdTomato C1 vector (#632564; Clontech) or pTSIN PGK-puro2 lentiviral vector. Lentiviral pFugW-HA-Ect2 cDNA was a kind gift from Dr. Alan Fields. TSIN-tdTomato-γtubulin, TSIN-H2B-mRFP and TSiN-H2B-YFP expression plasmids have all been previously described[28]. GFP-anillin (RhoA biosensor; Addgene #68026) was sub-cloned into pTSIN PGK-puro2 lentiviral vector. For generation of virus particles, the lentiviral vectors along with appropriate helper plasmids (1:1:1 molar ratio) were transfected into HEK-293T cells using Lipofectamine 2000 (#11668; Invitrogen). psPAX2 and pMD2G (pLKO.1), or VSV-G and pHR' CMV8.9 (pTSIN, pLVX and pFugW) were used as helper plasmids. After 48 h, supernatant containing virus particles was filtered through a 0.45 μm syringe filter, aliquoted and stored at −80 °C for further use.

Partial Hepatectomy

Partial hepatectomies were performed on 8-week-old male mice as previously described[59]. 50–52 h after surgery, mice were sacrificed and the liver lobes collected and fixed in PBS/4% paraformaldehyde (PFA) at 4°C for 24–48 h. Immunofluorescence analysis was performed as previously described[60]. 50–100 metaphases or anaphases per mouse were analyzed for assessments of misaligned or lagging chromosomes respectively.

Karyotype Analysis

Chromosome counts on colcemid-arrested MEFs or splenocytes from 5-month-old mice were performed as previously described[57]. For experiments assessing chromosome counts in MEFs after gene overexpression or knockdown, passage 2 (P2) MEFs were infected with lentivirus particles, selected with the appropriate antibiotic for 48 h and harvested at P5 for assessing the karyotype.

Live cell imaging

Chromosome segregation and mitotic timing analyses were performed on MEFs stably expressing H2B-mRFP as previously described[61]. Centrosome movement analysis was performed on MEFs stably expressing TSIN-H2B-YFP and TSIN-tdTomato-γTubulin. Cells were selected with duplicated centrosomes that were <3 μm apart and followed till nuclear envelope breakdown (NEBD). Images were taken at 3 min intervals. To obtain the speed of movement, the total distance covered by centrosomes at NEBD was divided by the time taken to cover that distance. 15–30 cells per line per genotype were used for analysis. Assessments of non-perpendicular spindles giving rise to chromosome lagging was performed as previously described[28]. For assessing RhoA activity, GFP-anillin (RhoA biosensor) was lentivirally introduced in MEFs. 2–3 min prior to imaging, complete DMEM media containing Hoechst 33342 (H1399; Molecular Probes, 1:10,000) was added to the cells to label DNA. Mitotic MEFs were imaged using an LSM 880 confocal microscope (Zeiss) with a heating unit and CO_2 module, within 20 min after changing media.

Indirect immunofluorescence and confocal microscopy

Immunofluorescence was performed as previously described[62]. For mitotic cortical actin and myosin staining, asynchronously growing cells were fixed in cytoskeleton stabilization buffer (CSB; 10 mM MES pH 6.1, 138 mM KCl, 3 mM $MgCl_2$, 2 mM EGTA, sucrose 0.32 M) or PBS/4% PFA for 20 min. For cortical actin staining in G_1 and G_2 phase, trypsinized MEFs were seeded on to slides and fixed after 30 min using CSB/4% PFA while they were still partially round. Cells were then permeabilized with PBS/0.2% Triton X-100 for 15 min and blocked with PBS/5% BSA for 60 min at RT. Cells were first labeled with phospho-histone-$H3^{Ser10}$, and subsequently incubated with TRITC-Phalloidin in PBS/5% BSA for 60 min. Cells were counterstained with Hoechst 33342 (0.01 mg/ml in PBS) and mounted using vectashield (Vector labs). Quantification of fluorescent signal was carried out using ImageJ version 1.49p (NIH) as previously described[62]. For quantification of cortical intensity, the mean cytoplasmic actin intensity per unit area was subtracted from the mean actin intensity per unit area of the entire cell. See Supplementary Table 5 for primary antibodies used. For all experiments, at least 3 independent cell lines and 15–25 cells per line were used for analysis. For centrosome movement analysis, the ratio of the distance between centrosomes to the nuclear diameter was measured at prophase. Cells with a ratio <0.45 were considered to have slow movement. All inhibitors/drugs were used on cells for 4 h prior to fixation. See Supplementary Table 5 for details.

Western Blot analysis, cell fractionation and co-immunoprecipitation

Western blot and co-immunoprecipitation (co-IP) analysis were performed as previously described[57]. All extracts were prepared in Laemmli buffer and boiled for 10 min. All experiments were performed at least 3 times. Sub-cellular fractionation was performed using the protein fractionation kit (78840; Thermo-Fisher) according to manufacturer's instructions. Densitometry quantification was performed using ImageJ (version 1.49p) software by measuring the area under the curve for the band intensity in each lane. See Supplementary Table 5 for a full list of antibodies used for western blot and immunoprecipitation.

Cell cycle analysis by flow cytometry

Asynchronously growing passage 4 MEFs were harvested at ~80% confluency, resuspended in 500 μl PBS, and fixed for 1 h or overnight by adding 500 μl ice-cold 95% ethanol. After fixation, cells were rehydrated and washed twice in PBS and incubated with RNaseA (1 mg/ml in PBS) for 15 min at 37°C. An equal volume of propidium iodide (100 μg/ml in 1% sodium citrate) was added. After 15 min incubation on ice shielded from light, cell cycle profiles were assessed by flow cytometry using a BD FACSCanto (>10,000 cells were analyzed). Flow cytometry data were analyzed with ModFit 5.0 software using a fitted model.

RNA isolation and quantitative PCR

RNA was extracted from asynchronously growing or mitotic MEFs and lung tissue from 10-day-old mice using the RNeasy Mini Kit (74104; Qiagen) according to manufacturer's instructions. cDNA synthesis (18080051; Invitrogen) and reverse-transcription quantitative

PCR (RT-qPCR) analysis (4309155; Applied Biosystems) were performed according to the manufacturers' instructions. The gene expression for each sample was normalized to *Actb*. The list of primers can be found in Supplementary Table 3.

RNA library preparation, sequencing and bioinformatics analyses

RNA library preparation, sequencing and downstream analysis was performed as previously described[60]. Genes were considered significantly differentially expressed when the false discovery rate (FDR) was < 0.05 and the Log_2 fold change > 0.3 or < −0.3. See Supplementary Table 1 and 2 for full list of DEGs. The FoxM1 downstream transcriptional target gene list was derived from Macedo et al[63]. These genes were considered targets when they were differentially expressed in *Foxm1*$^{+/-}$ versus *Foxm1*$^{+/+}$ and *Foxm1*$^{-/-}$ versus *Foxm1*$^{+/+}$ MEFs. Heatmaps were generated with Morpheus, Broad Institute (https://software.broadinstitue.org/morpheus) using Log_2 fold change values and Log_{10} (FDR) values.

Recombinant protein purification

To express Ect2 and FoxM1 deletion mutants as GST fusion proteins, cDNA was sub-cloned into pGEX-4T3 (GE Lifesciences). To express FoxM1$^{1–757}$ and FoxM1$^{1–232}$ as His-tag fusion proteins, cDNA was sub-cloned into pET28a (Novagen). All proteins were expressed in *E.* coli strain Rosetta-BL21(DE3) except for GST-Ect2$^{414–883}$ which was expressed in BL21-CodonPlus (DE3)- RIL cells (Agilent), by inducing at an O.D. of 0.8 using 1 mM IPTG (R0392; Thermo Scientific) for 4 h at 37°C. Bacteria were harvested in 10 ml PBS (for GST-tagged proteins) or 10 ml Nickel-A buffer (50 mM sodium phosphate, 300 mM NaCl, 5 mM imidazole, pH = 7.5) for His-tagged proteins, treated with lysozyme (1 mg/ml) for 20 min at RT and frozen at −80°C prior to protein purification. To purify proteins, 10 ml of ice-cold lysis buffer (0.25% NP-40, 20% glycerol in PBS for GST-tagged and Nickel-A buffer for His-tagged) containing protease inhibitors was added to the thawed bacterial pellet. The suspension was sonicated 7–8 times, followed by centrifugation at 50,000 g for 30 min. The supernatant was incubated with glutathione sepharose 4B beads (17075601; GE Lifesciences) or Ni-NTA agarose beads (30230; Qiagen) for 60 min at 4°C. Beads were washed 5 times in lysis buffer and captured proteins were directly used for experiments or eluted from the beads with GST elution buffer (50 mM Tris pH = 8, 10 mM reduced glutathione, 1 mM β-mercaptoethanol) or His-elution buffer (Nickel-A buffer with 300mM imidazole). All eluted proteins were concentrated and dialyzed against PBS using Vivaspin columns (28932248; GE Lifesciences) and stored at −80°C for future use.

In vitro binding assay

Mutant GST-Ect2 and His_6-FoxM1 recombinant proteins were purified as mentioned above. GST-Ect2 mutant proteins immobilized on beads were incubated with equal amounts of His-FoxM1$^{1–757}$ or His-FoxM1$^{1–232}$ recombinant protein in ice-cold IP buffer (10% glycerol, 0.1% NP-40 in PBS, pH = 7.4) containing protease inhibitors, in a final volume of 500 μl at 4^0C for 60 min with end over rotation. Beads were collected by centrifugation and washed 4 times with IP buffer. Proteins were eluted in 2X Laemmeli buffer and resolved on SDS-PAGE gels (4–15%; Bio-Rad), followed by western blot detection using antibodies against FoxM1 or His-tag (34660; Qiagen).

In vitro GEF exchange assay

In vitro GEF exchange activity of Ect2 towards RhoA was carried out using the RhoGEF exchange assay kit (BK-100; Cytoskeleton Inc.) according to manufacturer's instructions. 30 μg of Transiently overexpressed HA-Ect2 was immunoprecipitated from HEK-293T cells using 120 μl rat anti-HA beads. The beads were washed 5 times and resuspended in 100 μl of ddH_2O. 10 μl of the beads was incubated with recombinant GST or GST-$FoxM1^{1–232}$ proteins of different concentrations, for 30 min prior to use in the reaction. Readings were taken at 22–24°C for 60 min using a Tecan 2000 spectrophotometer. Three independent experiments were performed. Reactions containing only the buffer but not immunoprecipitated Ect2 served as negative control. Rates of nucleotide exchange for the different conditions were calculated by dividing the change in arbitrary fluorescence units (a.f.u.) of the reactions (a.f.u. at time = 60 min subtracted by a.f.u. at time = 0 min) over the time taken (60 min).

Active RhoA, Rac1 and Cdc42 assays

GTP-bound (active form) RhoA, Rac1 and Cdc42 from primary mammary tumor or MEF extracts was assessed by performing affinity purification using recombinant GST-RBD (Active RhoA) or GST-PBD (Active Rac1/Cdc42). Briefly, asynchronously growing MEFs or primary mammary tumors were lysed in ice-cold IP buffer containing protease inhibitors and centrifuged at 14,000 rpm for 20 min at 4°C. The supernatant was incubated with recombinant GST-PBD (MEFs) or GST-RBD (Tumors) immobilized on glutathione sepharose beads (as mentioned above) for 60 min at 4°C with end-over rotation. The beads were then collected and washed 4 times with IP buffer. Proteins were eluted in 2X Laemmeli buffer and resolved on SDS-PAGE gels (4–15%; Bio-Rad), followed by western blot detection of RhoA, Rac1 or Cdc42.

TCGA and TCPA Data Analysis

For generating the Kaplan-Meier survival curve correlating *FOXM1* gene expression to overall survival, the TCGA Colon and Rectal Cancer cohort (COADREAD) was selected and analyzed using the University of California, Santa Cruz Xena functional genomics browser (http://xenabrowser.net) [64]. *P* value and survival curve were generated by the software. The image showing *FOXM1* CNV in different TCGA cohorts was obtained directly from the TCGA GDC data portal https://portal.gdc.cancer.gov/genes/ENSG00000111206.

Gene expression of patient samples from TCGA projects were obtained from the UCSC Xena Functional Genomics Explorer (http://xenabrowser.net) in the form of FPKM-UQ. Samples in each cancer type were grouped based on FOXM1 expression: samples with FOXM1 level <= 15% were considered low-FOXM1 and those ≥85% high-FOXM1. Differential expression analysis between these 2 groups was performed using R package limma version 3.26.9[65]. For assessing enrichment of RhoA activated genes between the 2 groups, the Fisher's exact test was used to determine over-represented gene sets (Supplementary Table 4) in significantly down-regulated genes (FDR<0.5 and log fold-change ≤−1) in the FOXM1 high group. Boxplots were generated in GraphPad Prism 6 using the Tukey method. Heatmaps were generated using R package gplots version 3.0.1.1.

TCPA graphs and correlation analyses of FOXM1 and pYAP^{Ser127} presented in Fig. 7e and f are as extracted from the TCPA website https://tcpaportal.org/tcpa/correlation_analysis.html (no further data extraction or analysis was conducted).

Statistics and Reproducibility

GraphPad Prism 6 software was used performing all statistical tests. One-way ANOVA was always performed with Tukey's or Sidak's multiple comparisons test. No statistical test was used to pre-determine sample size but was determined based on previously published observations where significant differences were observed. No samples were excluded from the analyses. The experiments were not randomized. The investigators were not blinded during experimentation and outcome assessment.

Data Availability

RNA sequencing data have been deposited in the Gene Expression Omnibus under the accession number GSE130410. All source data have been provided as supplementary files. All other data supporting the findings of this study are available from the corresponding author on reasonable request.

Further information on research design is available in the Nature Research Reporting Summary linked to this article.

Extended Data

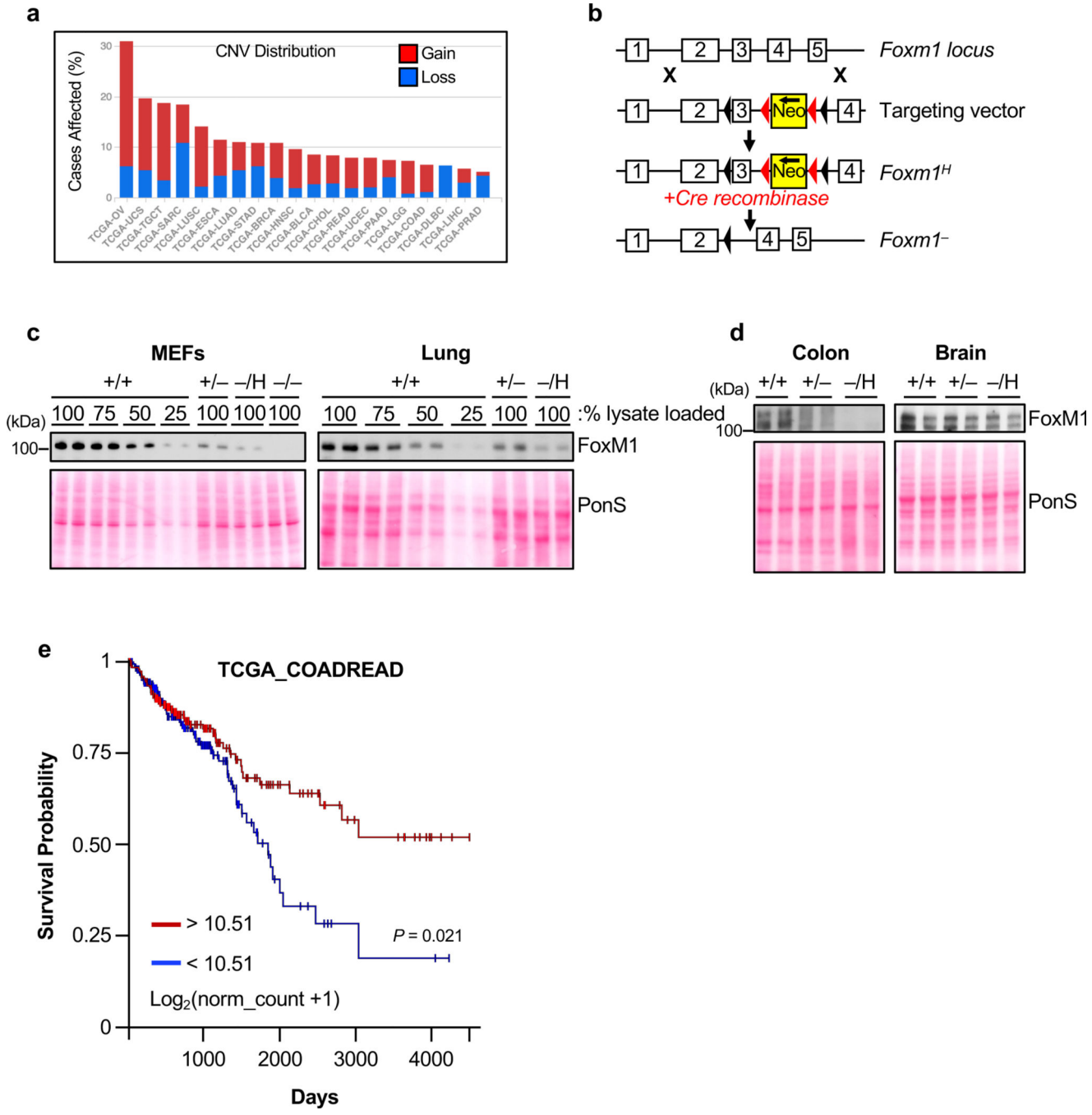

Extended Data Fig. 1. Generation of *Foxm1* knockout and hypomorphic alleles.

(a) Copy number variability (CNV) of the *FOXM1* gene in the indicated TCGA cohort. **(b)** Schematic representation of the gene targeting strategy used to generate *Foxm1* hypomorph (H) and knockout (−) alleles. **(c)** Quantification of FoxM1 protein levels in MEFs and lung tissue. PonS staining of blotted proteins was used as loading control. **(d)** Western blot analysis of FoxM1 in lysates of the indicated tissues. Western blots are representative of at

least 3 independent MEF lines or mice per genotype. **(e)** Overall survival analysis of human colorectal cancer patients from the TCGA COADREAD cohort with indicated *FOXM1* gene expression (n = 214 >10.51, n = 216 <10.51). Significance determined by Log Rank Test. See source file for uncropped immunoblots.

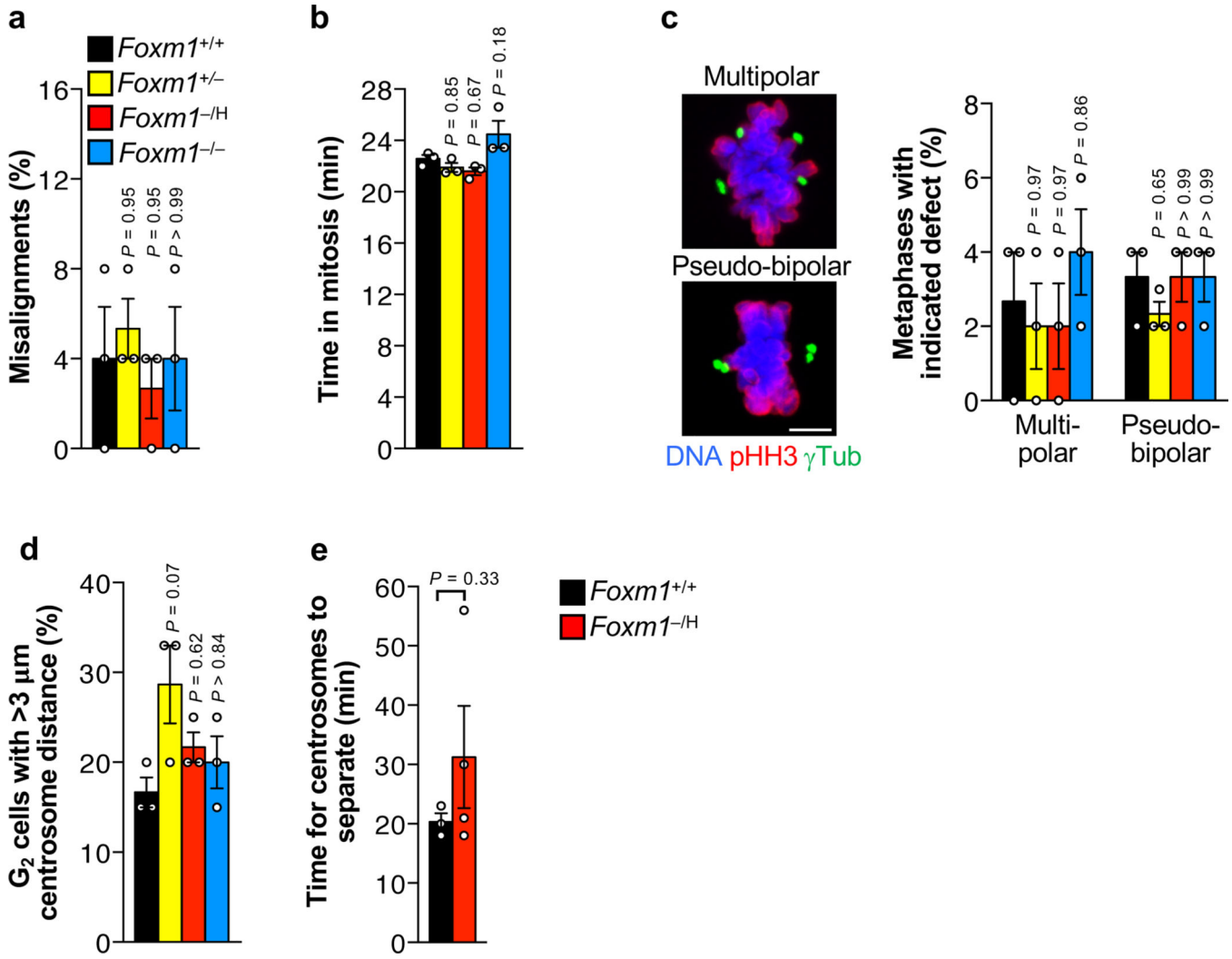

Extended Data Fig. 2. FoxM1 insufficiency does not perturb common CIN causing mechanisms.
(a) MEFs in metaphase with misaligned chromosomes after monastrol washout assay. (See methods). **(b)** Time taken from nuclear envelope breakdown (NEBD) to anaphase onset in MEFs expressing H2B-mRFP. **(c)** Quantification of MEFs with indicated spindle defect. **(d)** Quantification of G_2-phase cells with premature centrosome disjunction. (n = 3 independent MEF lines in **a-d**). **(e)** Time taken for centrosomes to separate after disjunction to NEBD in MEFs expressing H2B-YFP and γTubulin-tdTomato. (n = 3 +/+ and 4 −/H independent MEF lines). Data represent mean ± s.e.m. None of the analyses were statistically significant after performing one-way ANOVA with Tukey's correction **(a-d)** or two-tailed unpaired t-test **(e)**. See source file for original data.

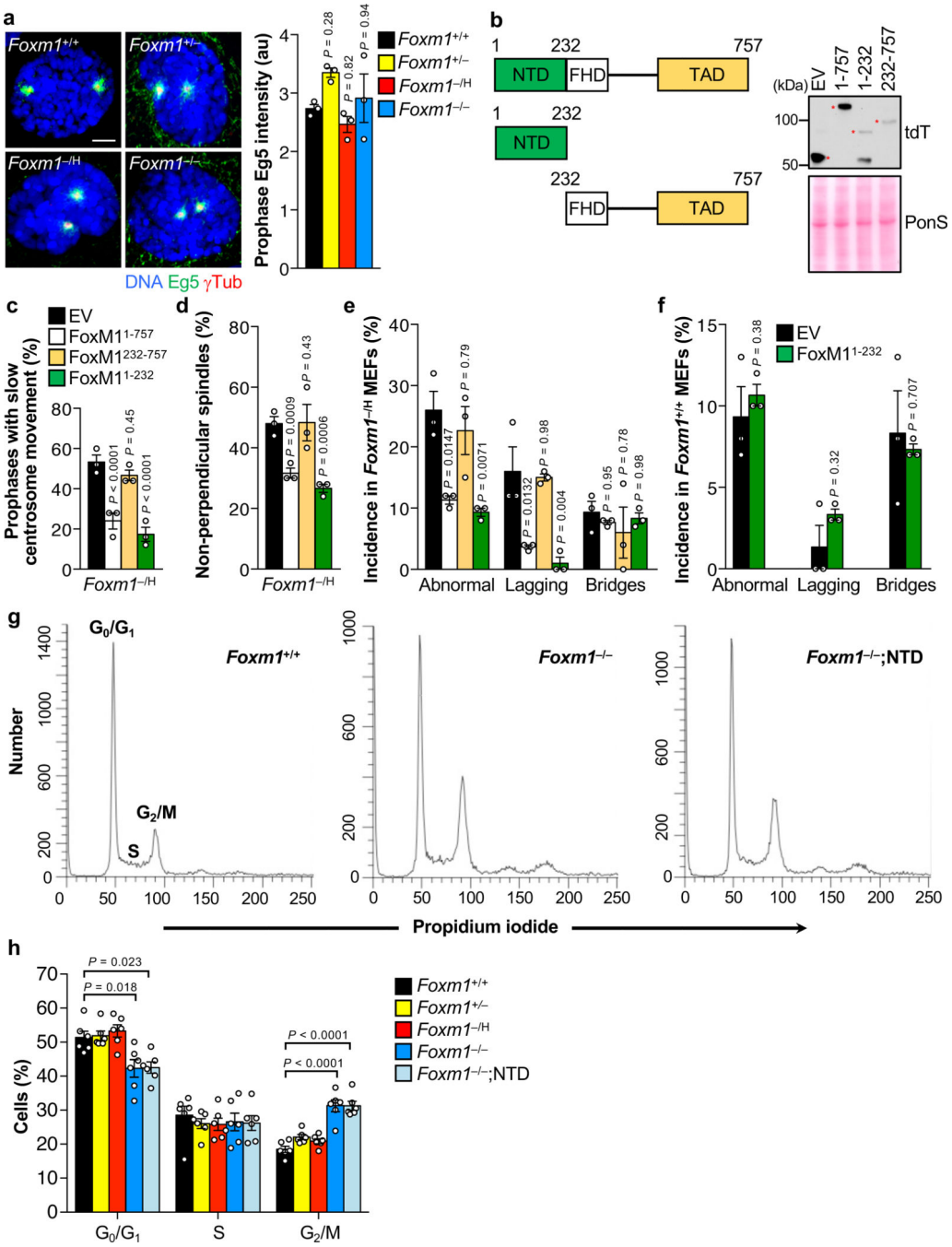

Extended Data Fig. 3. FoxM1 non-transcriptionally regulates centrosome movement independent of Eg5.

(a) Left: Images of MEFs in prophase immunostained for Eg5 and γtubulin. Right: Quantification of Eg5 signal at centrosomes. **(b)** Schematic representation and western blot analysis of tdTomato(tdT)-tagged FoxM1 cDNA constructs. N-terminal domain (NTD), Forkhead domain (FHD), Transactivation domain (TAD). Western blots are representative of 3 independent MEF lines per group. **(c)** Quantification of prophases with slow centrosome movement and **(d)** metaphases with non-perpendicular spindles in *Foxm1*$^{-/H}$

MEFs expressing indicated cDNA constructs. **(e)** Chromosome segregation analysis of MEFs expressing H2B-mRFP as in **c**. **(f)** Chromosome segregation analysis of *Foxm1*$^{+/+}$ MEFs stably expressing FoxM1$^{1–232}$. (n = 3 independent MEF lines per genotype in **a, c-f**). **(g)** Representative cell cycle profiles of the indicated propidium iodide-stained MEFs. **(h)** Quantification of cells in the indicated stage of the cell cycle as in **g**. (n = 6 independent MEF lines per genotype in **g, h**). Data represent mean ± s.e.m. Differences are not statistically significant in **a, f**. Statistics: **a, c-e, h** one-way ANOVA with Tukey's correction; **f**, two-tailed paired t-test. Scale bar, 5 μm. See source file for original data and uncropped immunoblots.

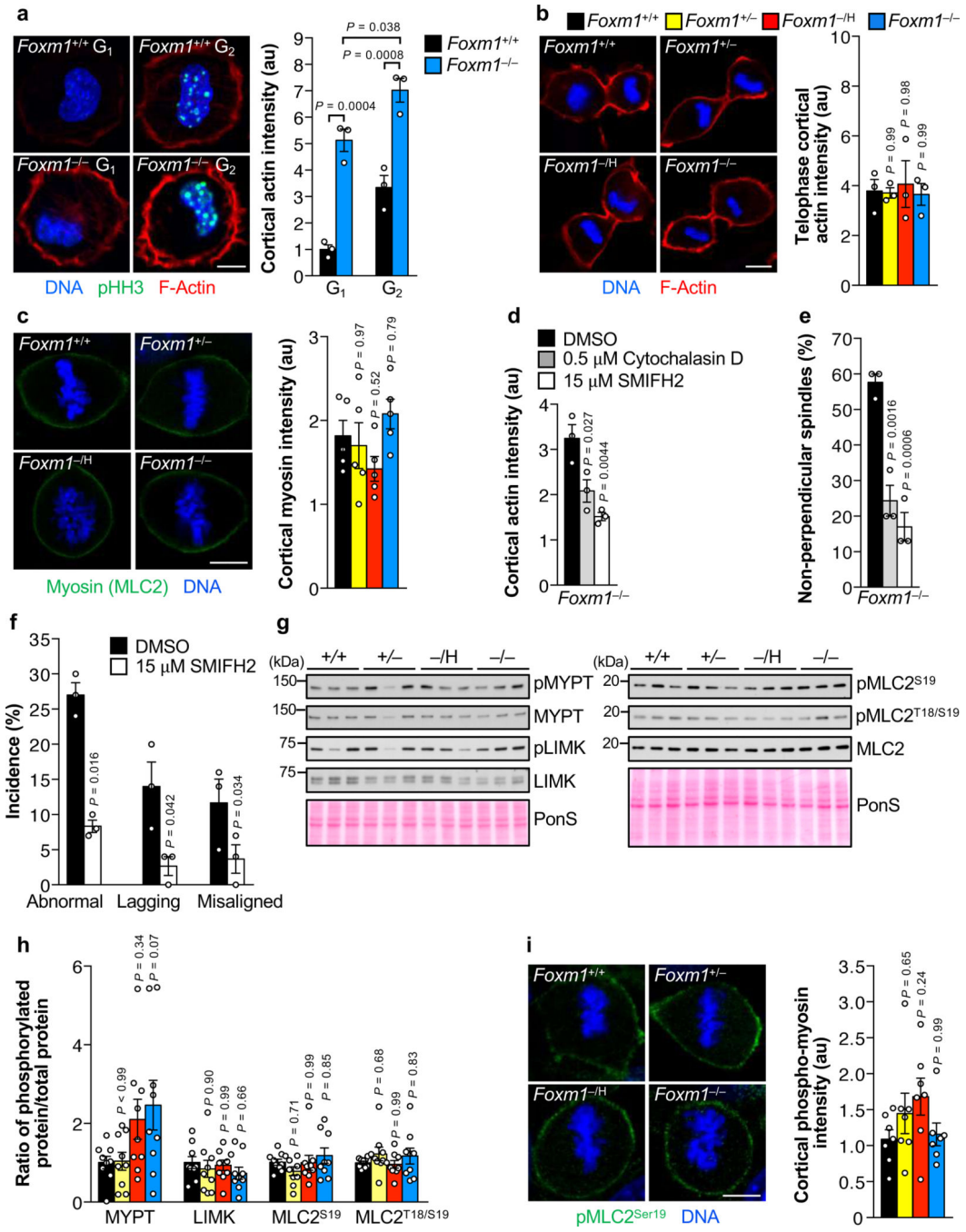

Extended Data Fig. 4. FoxM1 insufficiency does not hyperactivate ROCK-Myosin-II signaling.

(a) Left: Images of the indicated MEFs stained for TRITC-Phalloidin and phospho-histoneH3^{Ser10}. Right: Quantification of cortical actin intensity (n = 3 independent MEF lines). **(b)** Left: Images of the indicated MEFs stained with TRITC-Phalloidin. Right: Quantification of cortical actin intensity in telophase (n = 3 independent MEF lines) **(c)** Left: Images of MEFs stained for myosin light chain (MLC2). Right: Quantification of cortical MLC2 intensity (n = 5 independent MEF lines). **(d)** Quantification of cortical actin intensity and **(e)** non-perpendicular spindles in mitotic *Foxm1*$^{-/-}$ MEFs treated with the indicated

drugs for 4 h (n = 3 independent MEF lines). **(f)** Chromosome segregation analysis of MEFs as in **d**. **(g)** Western blot analysis of MEFs of the indicated genotypes. Western blots are representative of 3 independent experiments. **(h)** Densitometric quantification of band intensity of indicated proteins (n = 9 MEF lines analyzed across 3 independent experiments). **(i)** Left: Images of MEFs stained with phospho-myosin light chain (pMLC2^{Ser19}). Right: Quantification of cortical pMLC2 intensity (n = 7 independent MEF lines). Data represent mean ± s.e.m. Statistics: **a-e, h, i** one-way ANOVA with Tukey's correction; **f**, two-tailed paired t-test. Scale bars, 10 μm. See source file for original data and uncropped immunoblots.

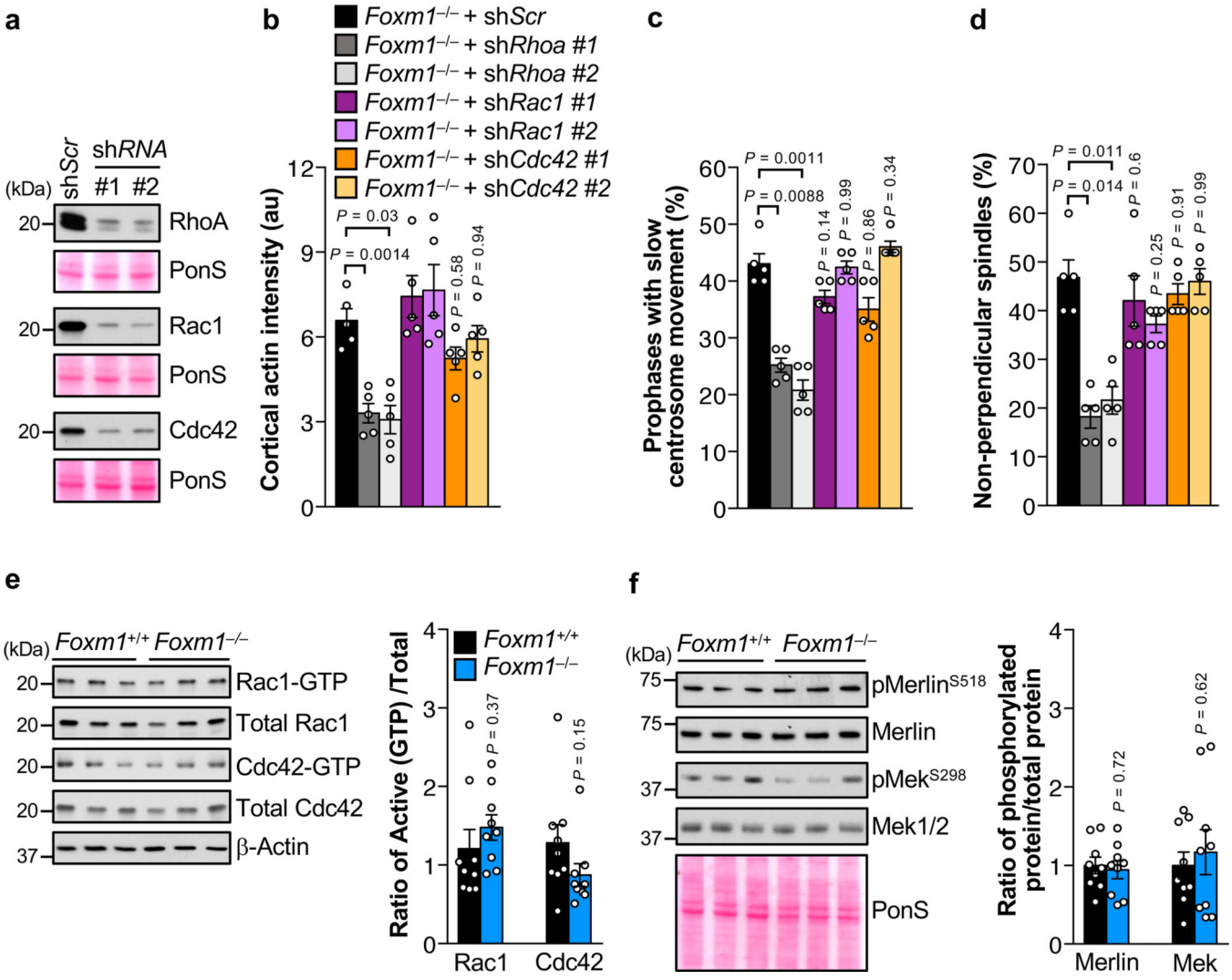

Extended Data Fig. 5. FoxM1 insufficiency does not alter Rac1 and Cdc42 Rho GTPases.
(a) Western blot analysis of *Foxm1*$^{-/-}$ MEFs lentivirally transduced with the indicated shRNAs. PonS staining was used as loading control. (**b-d**) *Foxm1*$^{-/-}$ MEFs stably expressing indicated shRNAs analyzed for cortical actin intensity **(b)**, incidence of slow centrosome movement in prophase **(c)**, and non-perpendicular spindles in metaphase **(d)** (n = 5 independent MEF lines in **b-d**). **(e)** Left: Western blot analysis of the indicated

MEF lysates. β-actin served as a loading control. Right: Densitometric quantification of signals from indicated proteins in the indicated MEFs (n = 9 MEF lines analyzed across 3 independent experiments). **(f)** Left: Western blot analysis of the indicated MEFs. PonS staining was used as loading control. Right: Densitometric quantification of signals from the indicated proteins (n = 9 MEF lines analyzed across 3 independent experiments). All western blots are representative of at least 3 independent experiments. Data represent mean ± s.e.m. Statistics: **b-d,** one-way ANOVA with Sidak's correction; **e, f**, two-tailed unpaired t-test. See source file for original data and uncropped immunoblots.

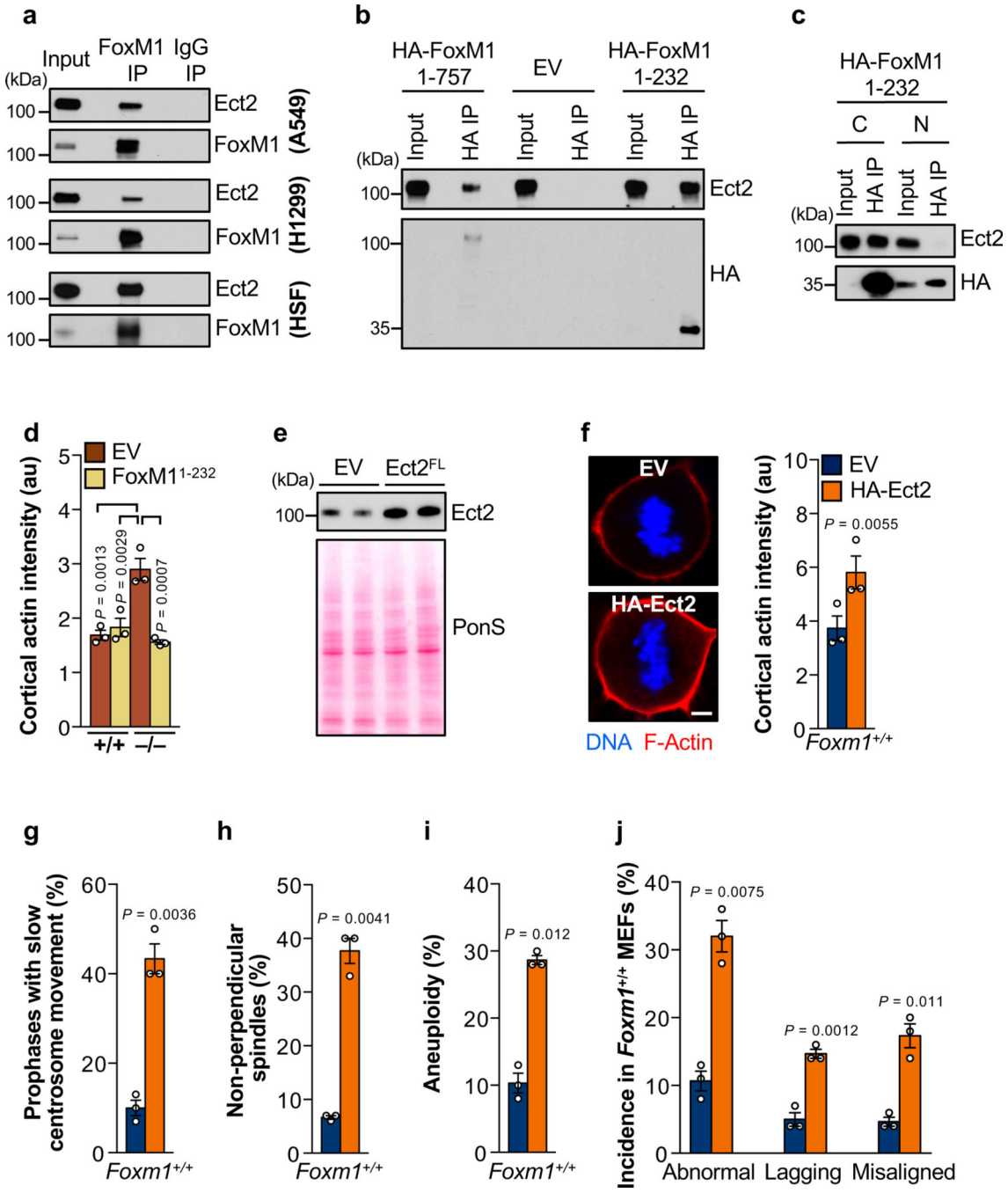

Extended Data Fig. 6. Ect2 overexpression phenocopies FoxM1 insufficiency.

(a) FoxM1 immunoprecipitation from A549 cells, H1299 cells and primary HSFs. **(b)** HA immunoprecipitation from whole-cell mitotic MEF extracts stably expressing indicated FoxM1 cDNA constructs. **(c)** HA immunoprecipitation from extracts of wildtype-MEFs stably expressing HA-FoxM1$^{1–232}$ subject to sub-cellular fractionation: C, cytoplasmic fraction; and N, nuclear fraction. **(d)** Quantification of cortical actin intensity in indicated MEFs stably expressing HA-FoxM1$^{1–1232}$ or empty vector (EV) (n = 3 independent MEF lines). **(e)** Western blot analysis of wildtype (WT) MEFs stably expressing empty-vector

(EV) or HA-Ect2. PonS served as loading control. **(f)** Left: Images of MEFs stained with TRITC-Phalloidin Right: Quantification of cortical actin intensity of MEFs as in **e** ($n = 3$ independent MEF lines). **(g)** Quantification of prophases with slow centrosome movement and **(h)** metaphases with non-perpendicular spindles as in **e.** ($n = 3$ independent MEF lines). **(i)** Chromosome counts and **(j)** chromosome segregation analysis of P5 MEFs as in **e.** ($n = 3$ independent MEF lines). All western blots are representative of at least 3 independent experiments or MEF lines.Data represent mean ± s.e.m. Statistics: **d,** one-way ANOVA with Tukey's correction; **f-j**, two-tailed paired *t*-test. Scale bar, 5 μm. See source file for original data and uncropped immunoblots.

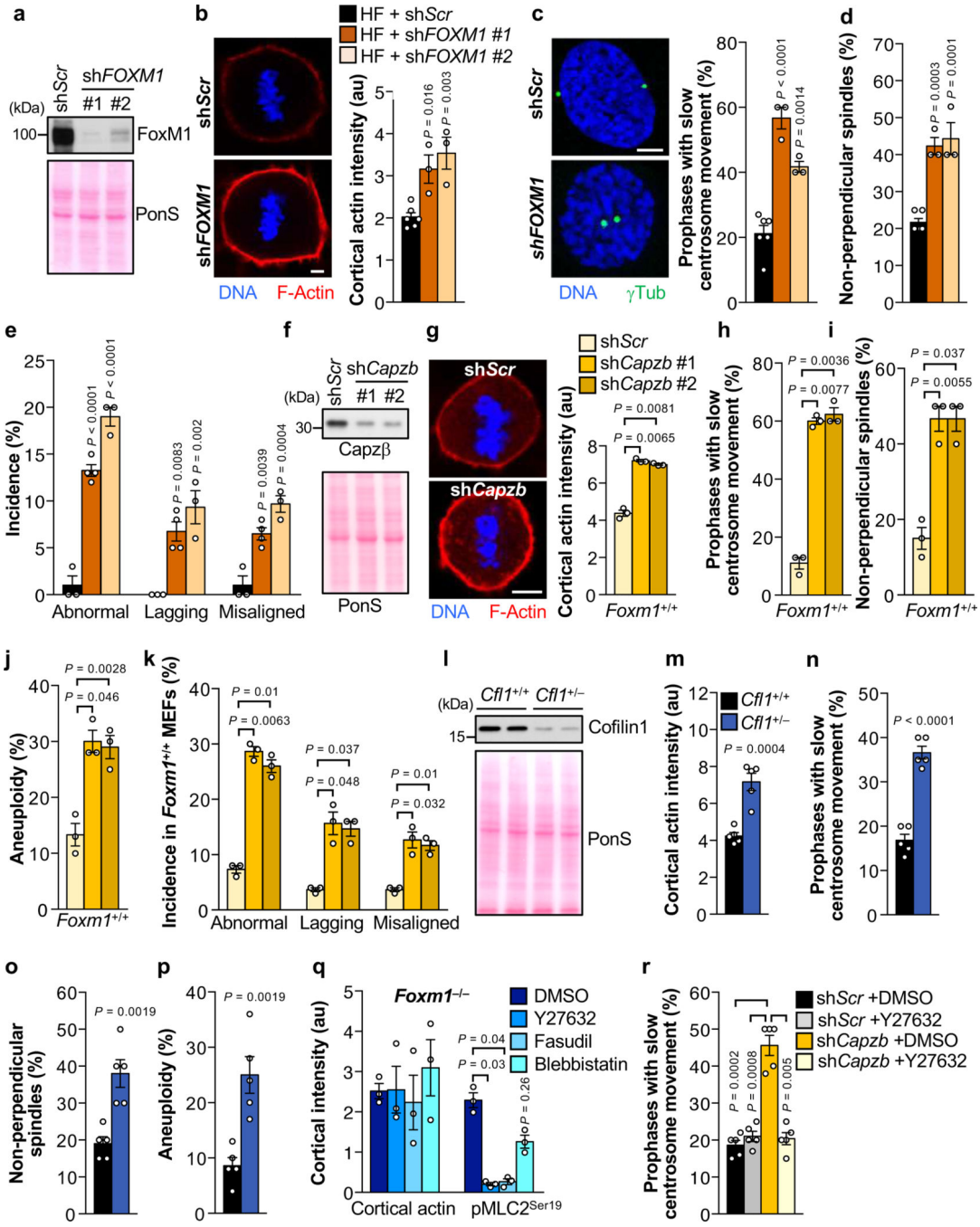

Extended Data Fig. 7. FoxM1-independent cortical actin hypernucleation slows centrosome movement and yields non-perpendicular spindles.

(a) Western blot analysis of primary HSFs lentivirally transduced with scramble (sh*Scr*) or two independent *FOXM1* shRNAs (sh*FOXM1*). PonS staining of blotted proteins served as loading control. **(b)** Left: Images of the indicated metaphases stained with TRITC-Phalloidin as in **a**. Right: Quantification of cortical actin intensity ($n = 3$ independent fibroblast lines for sh*FOXM1* groups and 6 independent lines for sh*Scr* group). **(c)** Left: Images of prophases immunostained with γtubulin as in **a**. Right: Quantification of prophases with

slow centrosome movement. (n = 3 independent fibroblast lines for sh*FOXM1* groups and 6 independent lines for sh*Scr* group). **(d)** Quantification of metaphases with non-perpendicular spindles as in **a**. (n = 3 independent fibroblast lines for sh*FOXM1* groups and 6 independent lines for sh*Scr* group). **(e)** Chromosome segregation analysis of HSFs expressing H2B-mRFP as in **a**. (n = 3 independent fibroblast lines for sh*Scr* and sh*FOXM1 #2* groups and 4 independent lines for sh*FOXM1 #1* group).**(f)** Western blot analysis of wildtype MEFs stably expressing the indicated shRNAs. **(g)** Left: Images of wildtype MEFs stably expressing the indicated shRNAs stained with TRITC-Phalloidin. Right: Quantification of cortical actin intensity in wildtype MEFs stably expressing the indicated shRNAs (n = 3 independent MEF lines). **(h-k)** Wildtype MEFs stably expressing the indicated shRNAs analyzed for slow centrosome movement in prophase **(h)**, non-perpendicular spindles in metaphase **(i)**, aneuploidy rates (chromosome counts on metaphase spreads) **(j)**, and chromosome segregation defects **(k)**. (n = 3 independent MEF lines). **(l)** Western blot analysis of the indicated MEFs. **(m-p)** Quantification of cortical actin intensity **(m),** quantification of prophases with slow centrosome movement **(n)**, metaphases with non-perpendicular spindles **(o)**, aneuploidy rates (chromosome counts on metaphase spreads) on the indicated P5 MEFs **(p)** (n= 5 independent MEF lines per genotype). **(q)** Quantification of cortical actin and cortical phospho-MLC2^{Ser19} intensity in *Foxm1*$^{-/-}$ MEFs after the indicated treatments for 4 h. (n = 3 independent MEF lines). **(r)** Quantification of prophases with slow centrosome movement of wildtype MEFs stably transduced with *scr* or *Capzb* shRNA, after treatment with 10 μM ROCK inhibitor Y-27632 for 4 h (n = 5 independent MEF lines). All western blots are representative of at least 3 HSF or MEF lines. Data represent mean ± s.e.m. Statistics: **b-k, q, r,** one-way ANOVA with Sidak's correction, **m-p,** two-tailed unpaired t-test. Scale bar, 5 μm. See source file for original data and uncropped immunoblots.

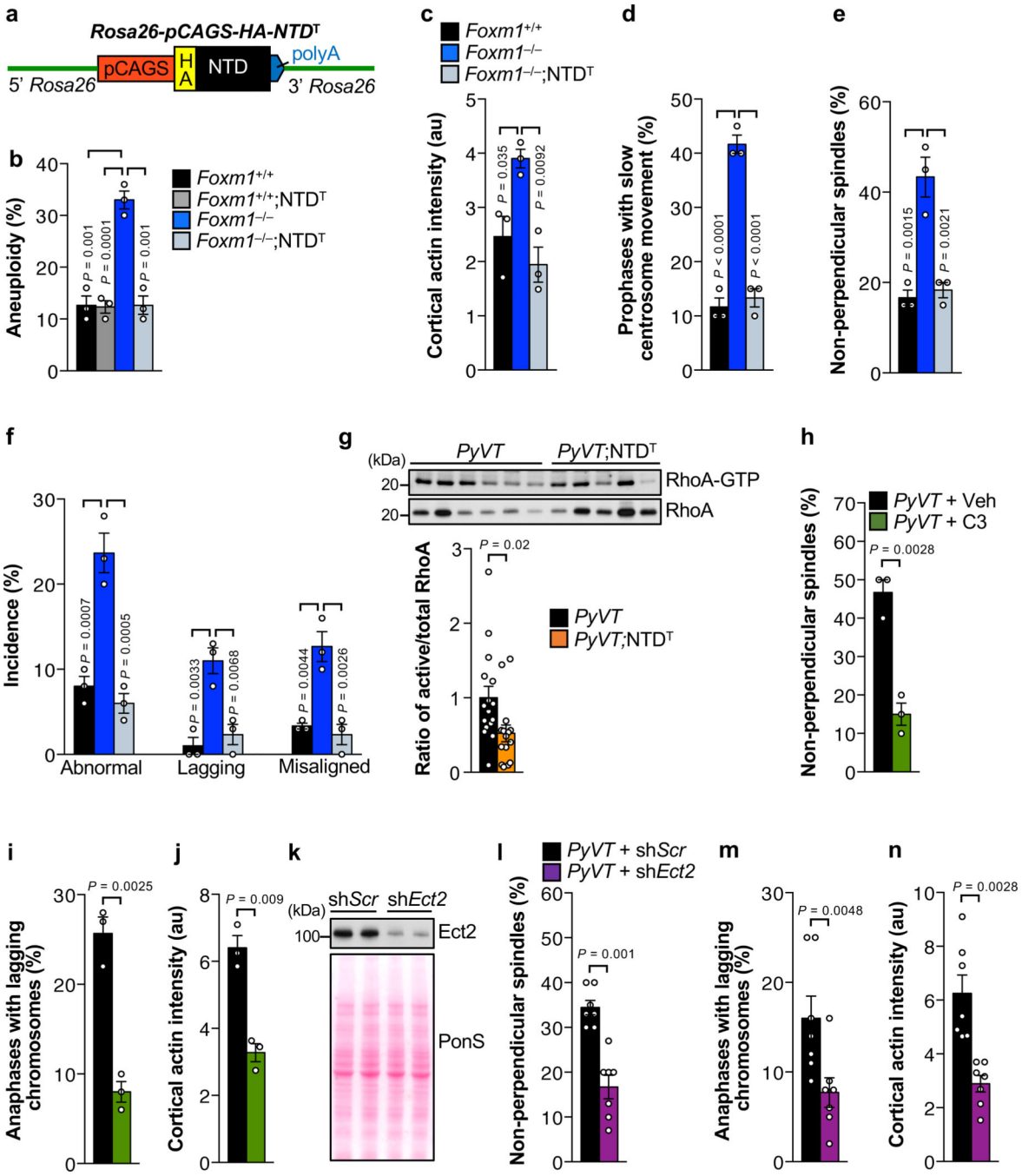

Extended Data Fig. 8. NTD^T corrects mitotic defects caused by Foxm1 insufficiency by inhibiting Ect2-RhoA signaling.

(a) Schematic for the generation of NTD^T mice. **(b)** Chromosome counts performed on MEFs of indicated genotypes (n = 3 independent MEF lines). **(c-f)** MEFs of indicated genotypes analyzed for cortical actin intensity in metaphase **(c)**, slow centrosome movement in prophase **(d),** non-perpendicular spindles in metaphase **(e)**, and chromosome segregation errors **(f)**. (n = 3 independent MEF lines). **(g)** Top:Western blot analysis of GTP-bound (active) and total RhoA in indicated mammary tumor extracts. Bottom: Densitometric

quantification of RhoA signals. (n = 16 *PyVT* and 15 *PyVT*; NTD^T tumors analyzed across 3 independent experiments). **(h-j)** Epithelial cells derived from MMTV-*PyVT* primary tumors, treated with vehicle (Veh) or 3 μg/ml RhoA inhibitor (C3) for 4 h and quantified for non-perpendicular spindles **(h)**, lagging chromosome incidence **(i)**, and cortical actin intensity **(j)**, (n = 3 independent tumor derived lines). **(k)** Western blot analysis of mammary epithelial tumor cells derived from MMTV-*PyVT* primary tumors lentivirally transduced with the indicated shRNAs. **(l-n)** MMTV-*PyVT* epithelial tumor cells quantified for non-perpendicular spindles **(l)**,lagging chromosome incidence **(m)**, and cortical actin intensity **(n).** (n = 7 independent tumor derived lines). All western blots are representative of at least 3 independent experiments or tumor lines. Data represent mean ± s.e.m. Statistics: **b-f,** one-way ANOVA with Tukey's correction; **g**, two-tailed unpaired *t*-test **h-n**, two-tailed paired *t*-test. See source file for original data and uncropped immunoblots.

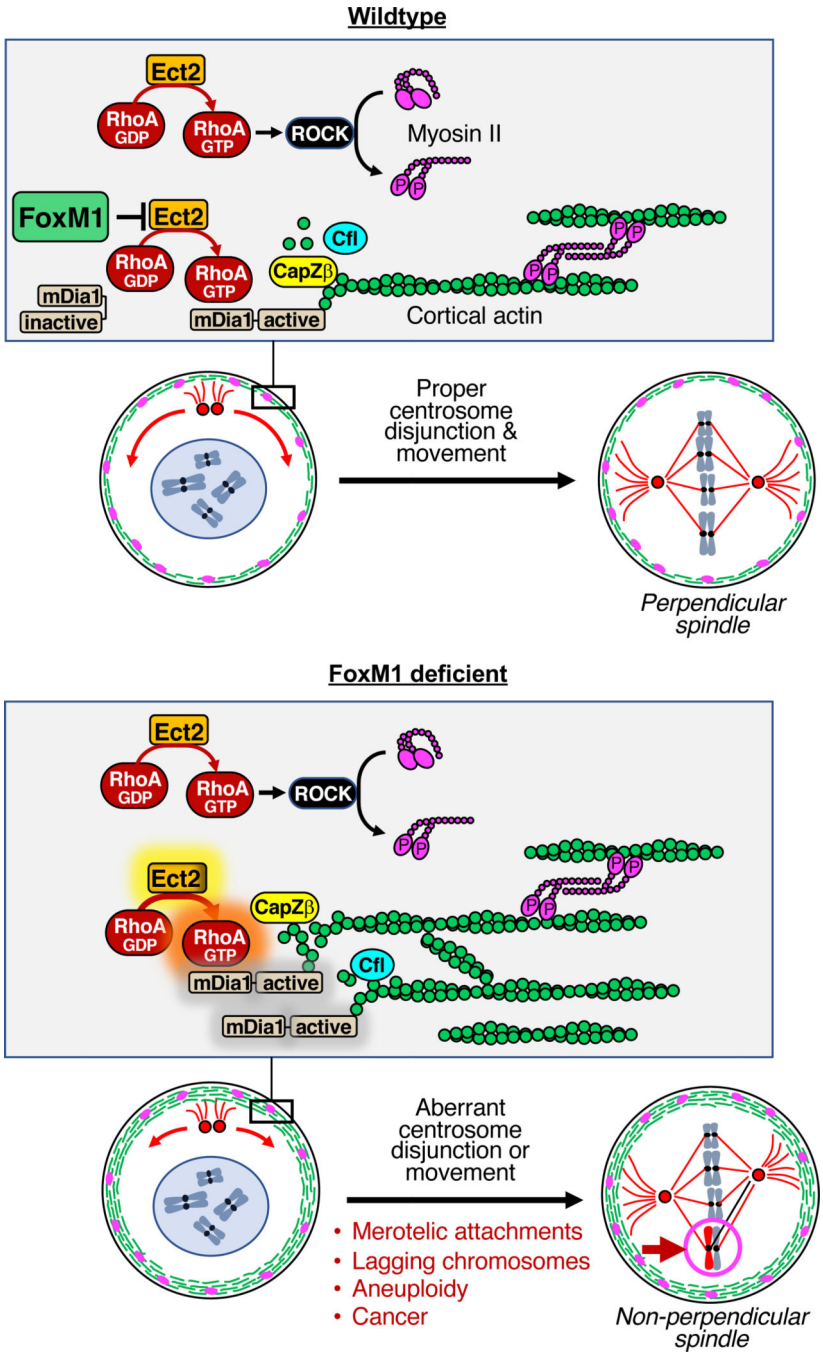

Extended Data Fig. 9. Hypothetical model for how FoxM1 controls cortical actin nucleation.

Ect2 hyperactivity has been linked to overactive Rho GTPases in human cancers. How Ect2 can become hyperactive remains incompletely understood. Here we identify FoxM1 as a key inhibitor of Ect2 activity and that its complete or partial loss results in increased signaling through the Ect2-RhoA-mDia- signaling axis. We find that FoxM1 binds to Ect2 via its NTD, thereby inhibiting Ect2-mediated activation of RhoA without impacting the activities of two other Rho GTPases, Rac1 and Cdc42 activity. RhoA regulates the actomyosin network through two effectors mDia1, which stimulates actin polymerization,

and ROCK which stimulates contractility through MLC activation and F-actin stabilization through LIMK (not shown). We find that FoxM1 selectively inhibits Ect2-mediated activation of mDia1, implying that RhoA activity toward ROCK is independently controlled. Cortical actin hypernucleation resulting from FoxM1 insufficiency slows movement of centrosomes along the cortex, yielding non-perpendicular spindles enriched for merotelic MT-kinetochore attachments that promote aneuploidization and providing a rate of genetic heterogeneity that stimulates tumor formation. FoxM1 independent mechanisms of cortical actin hypernucleation produce the same phenotype, which can be ameliorated by inhibiting myosin activity, indicating that rigidity of the actomyosin cortex is a key determinant of centrosome movement and spindle symmetry.

Supplementary Material

Refer to Web version on PubMed Central for supplementary material.

Acknowledgments:

The authors are grateful to B. Childs, R. Naylor and C. Sieben for helpful discussions, and G. Nelson for managing the mouse colony. We thank the transgenic and gene knockout core at Mayo Clinic for generation of all mutant mice strains, D. Billadeau (Mayo Clinic, Rochester) for the Cofilin 1 antibody, G. Razidlo (Mayo Clinic, Rochester) for Cytochalasin D and GST-PBD construct, S. Kaufmann (Mayo Clinic, Rochester) for H1299 and A549 cell lines and R. Thaler for assistance with the *in vitro* GEF activity assay. The human tumor results shown here are in whole or part based upon data generated by TCGA Research Network: https://www.cancer.gov/tcga.

Funding: This work was supported by NIH grants R01 CA096985, CA126828 and CA168709 to J.M.v.D. J.F.L is supported by Mayo Clinic Graduate School of Biomedical Sciences and J.A.K. by NIH T32 GM65841.

REFERENCES

1. Jaffe AB & Hall A. Rho GTPases: biochemistry and biology. Annu Rev Cell Dev Biol 21, 247–269, doi:10.1146/annurev.cellbio.21.020604.150721 (2005). [PubMed: 16212495]
2. Olson MF, Ashworth A. & Hall A. An essential role for Rho, Rac, and Cdc42 GTPases in cell cycle progression through G1. Science 269, 1270–1272, doi:10.1126/science.7652575 (1995). [PubMed: 7652575]
3. Gerhard R. et al. Glucosylation of Rho GTPases by Clostridium difficile toxin A triggers apoptosis in intestinal epithelial cells. J Med Microbiol 57, 765–770, doi:10.1099/jmm.0.47769-0 (2008). [PubMed: 18480335]
4. Provenzano PP & Keely PJ Mechanical signaling through the cytoskeleton regulates cell proliferation by coordinated focal adhesion and Rho GTPase signaling. J Cell Sci 124, 1195–1205, doi:10.1242/jcs.067009 (2011). [PubMed: 21444750]
5. Haga RB & Ridley AJ Rho GTPases: Regulation and roles in cancer cell biology. Small GTPases 7, 207–221, doi:10.1080/21541248.2016.1232583 (2016). [PubMed: 27628050]
6. Gomez del Pulgar T, Benitah SA, Valeron PF, Espina C. & Lacal JC Rho GTPase expression in tumourigenesis: evidence for a significant link. Bioessays 27, 602–613, doi:10.1002/bies.20238 (2005). [PubMed: 15892119]
7. Horiuchi A. et al. Up-regulation of small GTPases, RhoA and RhoC, is associated with tumor progression in ovarian carcinoma. Lab Invest 83, 861–870 (2003). [PubMed: 12808121]
8. Li XR et al. Overexpression of RhoA is associated with poor prognosis in hepatocellular carcinoma. Eur J Surg Oncol 32, 1130–1134, doi:10.1016/j.ejso.2006.05.012 (2006). [PubMed: 16806792]
9. Kamai T. et al. Overexpression of RhoA, Rac1, and Cdc42 GTPases is associated with progression in testicular cancer. Clin Cancer Res 10, 4799–4805, doi:10.1158/1078-0432.CCR-0436-03 (2004). [PubMed: 15269155]

10. Engers R. et al. Prognostic relevance of increased Rac GTPase expression in prostate carcinomas. Endocr Relat Cancer 14, 245–256, doi:10.1677/ERC-06-0036 (2007). [PubMed: 17639041]
11. Orgaz JL, Herraiz C. & Sanz-Moreno V. Rho GTPases modulate malignant transformation of tumor cells. Small GTPases 5, e29019, doi:10.4161/sgtp.29019 (2014).
12. Porter AP, Papaioannou A. & Malliri A. Deregulation of Rho GTPases in cancer. Small GTPases 7, 123–138, doi:10.1080/21541248.2016.1173767 (2016). [PubMed: 27104658]
13. Fields AP & Justilien V. The guanine nucleotide exchange factor (GEF) Ect2 is an oncogene in human cancer. Adv Enzyme Regul 50, 190–200, doi:10.1016/j.advenzreg.2009.10.010 (2010). [PubMed: 19896966]
14. Tatsumoto T, Xie X, Blumenthal R, Okamoto I. & Miki T. Human ECT2 is an exchange factor for Rho GTPases, phosphorylated in G2/M phases, and involved in cytokinesis. J Cell Biol 147, 921–928, doi:10.1083/jcb.147.5.921 (1999). [PubMed: 10579713]
15. Bandla S. et al. Comparative genomics of esophageal adenocarcinoma and squamous cell carcinoma. Ann Thorac Surg 93, 1101–1106, doi:10.1016/j.athoracsur.2012.01.064 (2012). [PubMed: 22450065]
16. Sonoda G. et al. Comparative genomic hybridization detects frequent overrepresentation of chromosomal material from 3q26, 8q24, and 20q13 in human ovarian carcinomas. Genes Chromosomes Cancer 20, 320–328 (1997). [PubMed: 9408747]
17. Kim JE, Billadeau DD & Chen J. The tandem BRCT domains of Ect2 are required for both negative and positive regulation of Ect2 in cytokinesis. J Biol Chem 280, 5733–5739, doi:10.1074/jbc.M409298200 (2005). [PubMed: 15545273]
18. Justilien V, Jameison L, Der CJ, Rossman KL & Fields AP Oncogenic activity of Ect2 is regulated through protein kinase C iota-mediated phosphorylation. J Biol Chem 286, 8149–8157, doi:10.1074/jbc.M110.196113 (2011). [PubMed: 21189248]
19. Saito S. et al. Deregulation and mislocalization of the cytokinesis regulator ECT2 activate the Rho signaling pathways leading to malignant transformation. J Biol Chem 279, 7169–7179, doi:10.1074/jbc.M306725200 (2004). [PubMed: 14645260]
20. Justilien V. et al. Ect2-Dependent rRNA Synthesis Is Required for KRAS-TRP53-Driven Lung Adenocarcinoma. Cancer Cell 31, 256–269, doi:10.1016/j.ccell.2016.12.010 (2017). [PubMed: 28110998]
21. Laoukili J. et al. FoxM1 is required for execution of the mitotic programme and chromosome stability. Nat Cell Biol 7, 126–136, doi:10.1038/ncb1217 (2005). [PubMed: 15654331]
22. Pilarsky C, Wenzig M, Specht T, Saeger HD & Grutzmann R. Identification and validation of commonly overexpressed genes in solid tumors by comparison of microarray data. Neoplasia 6, 744–750, doi:10.1593/neo.04277 (2004). [PubMed: 15720800]
23. Halasi M. & Gartel AL Targeting FOXM1 in cancer. Biochem Pharmacol 85, 644–652, doi:10.1016/j.bcp.2012.10.013 (2013). [PubMed: 23103567]
24. Barger CJ, Branick C, Chee L. & Karpf AR Pan-Cancer Analyses Reveal Genomic Features of FOXM1 Overexpression in Cancer. Cancers (Basel) 11, doi:10.3390/cancers11020251 (2019).
25. Krupczak-Hollis K. et al. The mouse Forkhead Box m1 transcription factor is essential for hepatoblast mitosis and development of intrahepatic bile ducts and vessels during liver morphogenesis. Dev Biol 276, 74–88, doi:10.1016/j.ydbio.2004.08.022 (2004). [PubMed: 15531365]
26. Thompson SL, Bakhoum SF & Compton DA Mechanisms of chromosomal instability. Curr Biol 20, R285–295, doi:10.1016/j.cub.2010.01.034 (2010). [PubMed: 20334839]
27. Nam HJ, Naylor RM & van Deursen JM Centrosome dynamics as a source of chromosomal instability. Trends Cell Biol 25, 65–73, doi:10.1016/j.tcb.2014.10.002 (2015). [PubMed: 25455111]
28. Kanakkanthara A. et al. Cyclin A2 is an RNA binding protein that controls Mre11 mRNA translation. Science 353, 1549–1552, doi:10.1126/science.aaf7463 (2016). [PubMed: 27708105]
29. van Ree JH, Nam HJ, Jeganathan KB, Kanakkanthara A. & van Deursen JM Pten regulates spindle pole movement through Dlg1-mediated recruitment of Eg5 to centrosomes. Nat Cell Biol 18, 814–821, doi:10.1038/ncb3369 (2016). [PubMed: 27240320]

30. Park HJ et al. An N-terminal inhibitory domain modulates activity of FoxM1 during cell cycle. Oncogene 27, 1696–1704, doi:10.1038/sj.onc.1210814 (2008). [PubMed: 17891172]
31. Laoukili J. et al. Activation of FoxM1 during G2 requires cyclin A/Cdk-dependent relief of autorepression by the FoxM1 N-terminal domain. Mol Cell Biol 28, 3076–3087, doi:10.1128/MCB.01710-07 (2008). [PubMed: 18285455]
32. Chugh P. & Paluch EK The actin cortex at a glance. J Cell Sci 131, doi:10.1242/jcs.186254 (2018).
33. Rosenblatt J, Cramer LP, Baum B. & McGee KM Myosin II-dependent cortical movement is required for centrosome separation and positioning during mitotic spindle assembly. Cell 117, 361–372 (2004). [PubMed: 15109496]
34. Bovellan M. et al. Cellular control of cortical actin nucleation. Curr Biol 24, 1628–1635, doi:10.1016/j.cub.2014.05.069 (2014). [PubMed: 25017211]
35. Matthews HK et al. Changes in Ect2 localization couple actomyosin-dependent cell shape changes to mitotic progression. Dev Cell 23, 371–383, doi:10.1016/j.devcel.2012.06.003 (2012). [PubMed: 22898780]
36. Basant A. & Glotzer M. Spatiotemporal Regulation of RhoA during Cytokinesis. Curr Biol 28, R570–R580, doi:10.1016/j.cub.2018.03.045 (2018). [PubMed: 29738735]
37. Piekny AJ & Glotzer M. Anillin is a scaffold protein that links RhoA, actin, and myosin during cytokinesis. Curr Biol 18, 30–36, doi:10.1016/j.cub.2007.11.068 (2008). [PubMed: 18158243]
38. Chugh P. et al. Actin cortex architecture regulates cell surface tension. Nat Cell Biol 19, 689–697, doi:10.1038/ncb3525 (2017). [PubMed: 28530659]
39. Foster CT, Gualdrini F. & Treisman R. Mutual dependence of the MRTF-SRF and YAP-TEAD pathways in cancer-associated fibroblasts is indirect and mediated by cytoskeletal dynamics. Genes Dev 31, 2361–2375, doi:10.1101/gad.304501.117 (2017). [PubMed: 29317486]
40. Yu OM et al. YAP and MRTF-A, transcriptional co-activators of RhoA-mediated gene expression, are critical for glioblastoma tumorigenicity. Oncogene 37, 5492–5507, doi:10.1038/s41388-018-0301-5 (2018). [PubMed: 29887596]
41. Wang Y. et al. Comprehensive Molecular Characterization of the Hippo Signaling Pathway in Cancer. Cell Rep 25, 1304–1317 e1305, doi:10.1016/j.celrep.2018.10.001 (2018). [PubMed: 30380420]
42. Oka T, Mazack V. & Sudol M. Mst2 and Lats kinases regulate apoptotic function of Yes kinase-associated protein (YAP). J Biol Chem 283, 27534–27546, doi:10.1074/jbc.M804380200 (2008). [PubMed: 18640976]
43. Dupont S. et al. Role of YAP/TAZ in mechanotransduction. Nature 474, 179–183, doi:10.1038/nature10137 (2011). [PubMed: 21654799]
44. Feng X. et al. Hippo-independent activation of YAP by the GNAQ uveal melanoma oncogene through a trio-regulated rho GTPase signaling circuitry. Cancer Cell 25, 831–845, doi:10.1016/j.ccr.2014.04.016 (2014). [PubMed: 24882515]
45. Guy CT, Cardiff RD & Muller WJ Induction of mammary tumors by expression of polyomavirus middle T oncogene: a transgenic mouse model for metastatic disease. Mol Cell Biol 12, 954–961 (1992). [PubMed: 1312220]
46. Nobis M. et al. A RhoA-FRET Biosensor Mouse for Intravital Imaging in Normal Tissue Homeostasis and Disease Contexts. Cell Rep 21, 274–288, doi:10.1016/j.celrep.2017.09.022 (2017). [PubMed: 28978480]
47. Glotzer M. The molecular requirements for cytokinesis. Science 307, 1735–1739, doi:10.1126/science.1096896 (2005). [PubMed: 15774750]
48. Fields AP, Ali SA, Justilien V. & Murray NR Protein kinase Ciota: A versatile oncogene in the lung. Mol Cell Oncol 5, e1190886, doi:10.1080/23723556.2016.1190886 (2018).
49. Thompson LL, Jeusset LM, Lepage CC & McManus KJ Evolving Therapeutic Strategies to Exploit Chromosome Instability in Cancer. Cancers (Basel) 9, doi:10.3390/cancers9110151 (2017).
50. Chan KS, Koh CG & Li HY Mitosis-targeted anti-cancer therapies: where they stand. Cell Death Dis 3, e411, doi:10.1038/cddis.2012.148 (2012). [PubMed: 23076219]
51. Bakhoum SF et al. Chromosomal instability drives metastasis through a cytosolic DNA response. Nature 553, 467–472, doi:10.1038/nature25432 (2018). [PubMed: 29342134]

52. Bolhaqueiro ACF et al. Ongoing chromosomal instability and karyotype evolution in human colorectal cancer organoids. Nat Genet 51, 824–834, doi:10.1038/s41588-0190399-6 (2019). [PubMed: 31036964]

53. Burrell RA & Swanton C. Tumour heterogeneity and the evolution of polyclonal drug resistance. Mol Oncol 8, 1095–1111, doi:10.1016/j.molonc.2014.06.005 (2014). [PubMed: 25087573]

54. Jamal-Hanjani M. et al. Tracking the Evolution of Non-Small-Cell Lung Cancer. N Engl J Med 376, 2109–2121, doi:10.1056/NEJMoa1616288 (2017). [PubMed: 28445112]

55. McGranahan N. & Swanton C. Biological and therapeutic impact of intratumor heterogeneity in cancer evolution. Cancer Cell 27, 15–26, doi:10.1016/j.ccell.2014.12.001 (2015). [PubMed: 25584892]

56. Turajlic S. & Swanton C. Metastasis as an evolutionary process. Science 352, 169–175, doi:10.1126/science.aaf2784 (2016). [PubMed: 27124450]

57. Babu JR et al. Rae1 is an essential mitotic checkpoint regulator that cooperates with Bub3 to prevent chromosome missegregation. J Cell Biol 160, 341–353, doi:10.1083/jcb.200211048 (2003). [PubMed: 12551952]

58. Moffat J. et al. A lentiviral RNAi library for human and mouse genes applied to an arrayed viral high-content screen. Cell 124, 1283–1298, doi:10.1016/j.cell.2006.01.040 (2006). [PubMed: 16564017]

59. Mitchell C. & Willenbring H. A reproducible and well-tolerated method for 2/3 partial hepatectomy in mice. Nat Protoc 3, 1167–1170, doi:10.1038/nprot.2008.80 (2008). [PubMed: 18600221]

60. Aziz K. et al. Ccne1 Overexpression Causes Chromosome Instability in Liver Cells and Liver Tumor Development in Mice. Gastroenterology, doi:10.1053/j.gastro.2019.03.016 (2019).

61. Jeganathan KB, Malureanu L. & van Deursen JM The Rae1-Nup98 complex prevents aneuploidy by inhibiting securin degradation. Nature 438, 1036–1039, doi:10.1038/nature04221 (2005). [PubMed: 16355229]

62. Nam HJ & van Deursen JM Cyclin B2 and p53 control proper timing of centrosome separation. Nat Cell Biol 16, 538–549, doi:10.1038/ncb2952 (2014). [PubMed: 24776885]

63. Macedo JC et al. FoxM1 repression during human aging leads to mitotic decline and aneuploidy-driven full senescence. Nat Commun 9, 2834, doi:10.1038/s41467-01805258-6 (2018). [PubMed: 30026603]

64. Goldman M. et al. The UCSC Xena platform for public and private cancer genomics data visualization and interpretation. bioRxiv, 326470, doi:10.1101/326470 (2019).

65. Ritchie ME et al. limma powers differential expression analyses for RNA-sequencing and microarray studies. Nucleic Acids Res 43, e47, doi:10.1093/nar/gkv007 (2015). [PubMed: 25605792]

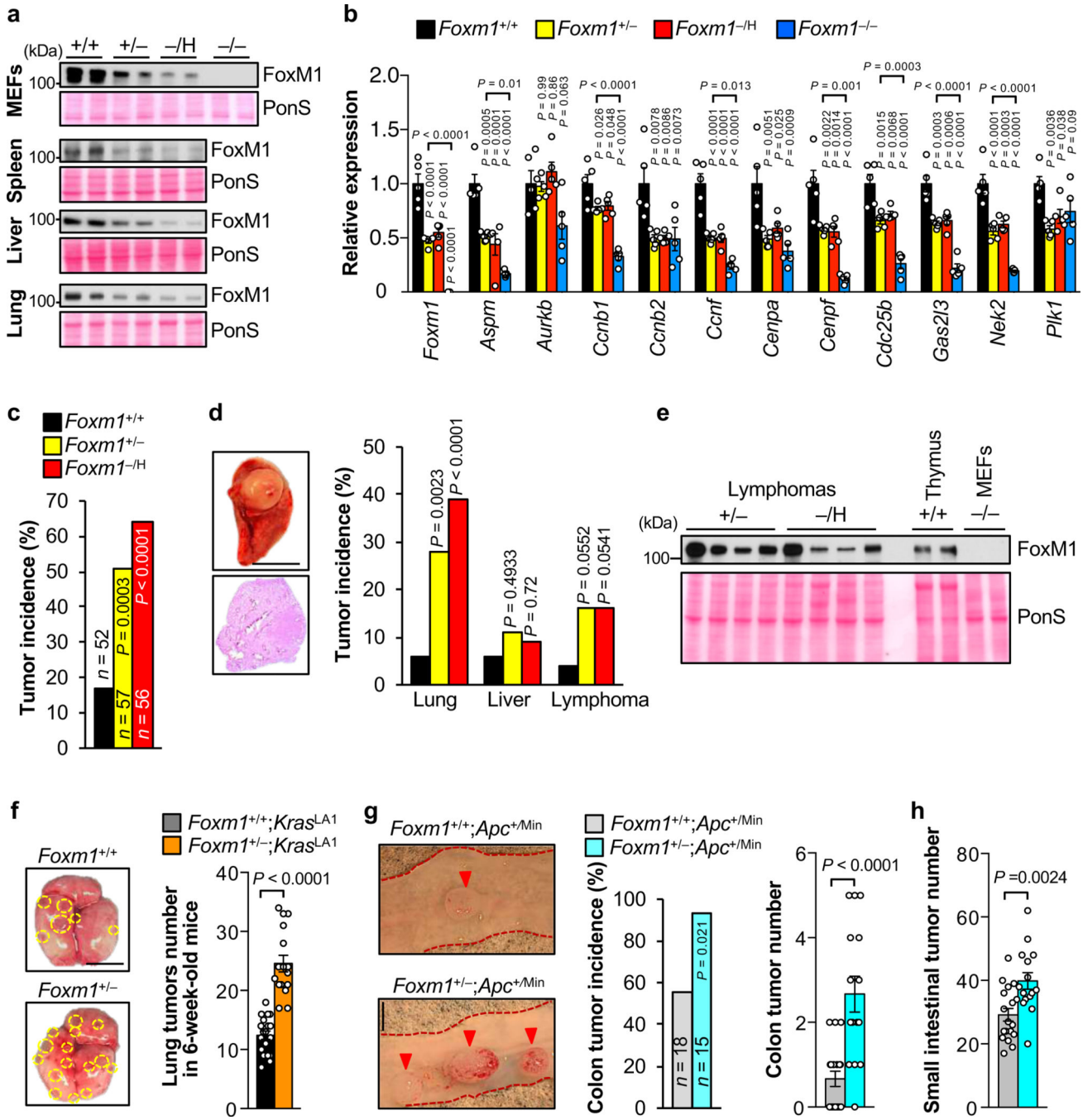

Figure 1. FoxM1 insufficiency causes tumor formation.

(a) Western blot analysis of lysates from MEFs and indicated tissues of *Foxm1*$^{+/+}$ (+/+), *Foxm1*$^{+/-}$(+/−), *Foxm1*$^{-/H}$ (−/H) and *Foxm1*$^{-/-}$ (−/−) mice. Ponceau S (PonS) staining of blotted proteins served as a loading control. All western blots are representative of at least 3 independent MEF lines or mice per group. **(b)** Analysis of mitotic MEFs of the indicated genotypes for transcript levels of established FoxM1 target genes using RT-qPCR (n = 5 independent MEF lines per group). **(c)** Spontaneous tumor incidence in 16-month-old mice (n = 52 +/+, 57 +/−, and 56 −/H mice). **(d)** Left: Representative image and histological

analysis of an observed lung tumor. Right:Spectrum of spontaneous tumors observed in cohorts indicated in **c**. **(e)** Western blot analysis of lymphoma lysates from 16-month-old mice of the indicated genotypes. PonS staining of blotted proteins served as a loading control. **(f)** Representative images and multiplicity of lung tumors in 6-week-old mice on the *Kras*^{LA1} background (n = 19 +/+ and 16 +/− mice). **(g)** Left:Representative images of colon tumors in 90-day-old mice on *Apc*$^{+/Min}$ background. Right: Incidence and multiplicity of colon tumors of mice on *Apc*$^{+/Min}$ background (n = 18 +/+ and 15 +/− mice). **(h)** Multiplicity of small intestinal tumors as in **g**. Data in **b**, **f-h** represent mean ± s.e.m. Statistics: **b**, one-way ANOVA with Tukey's correction; **c, d, g (incidence)**, two-tailed Fisher's exact test; **f-h**, two-tailed unpaired *t*-test. Scale bars: **d, f, g**, 5 mm. See source file for original data and uncropped immunoblots.

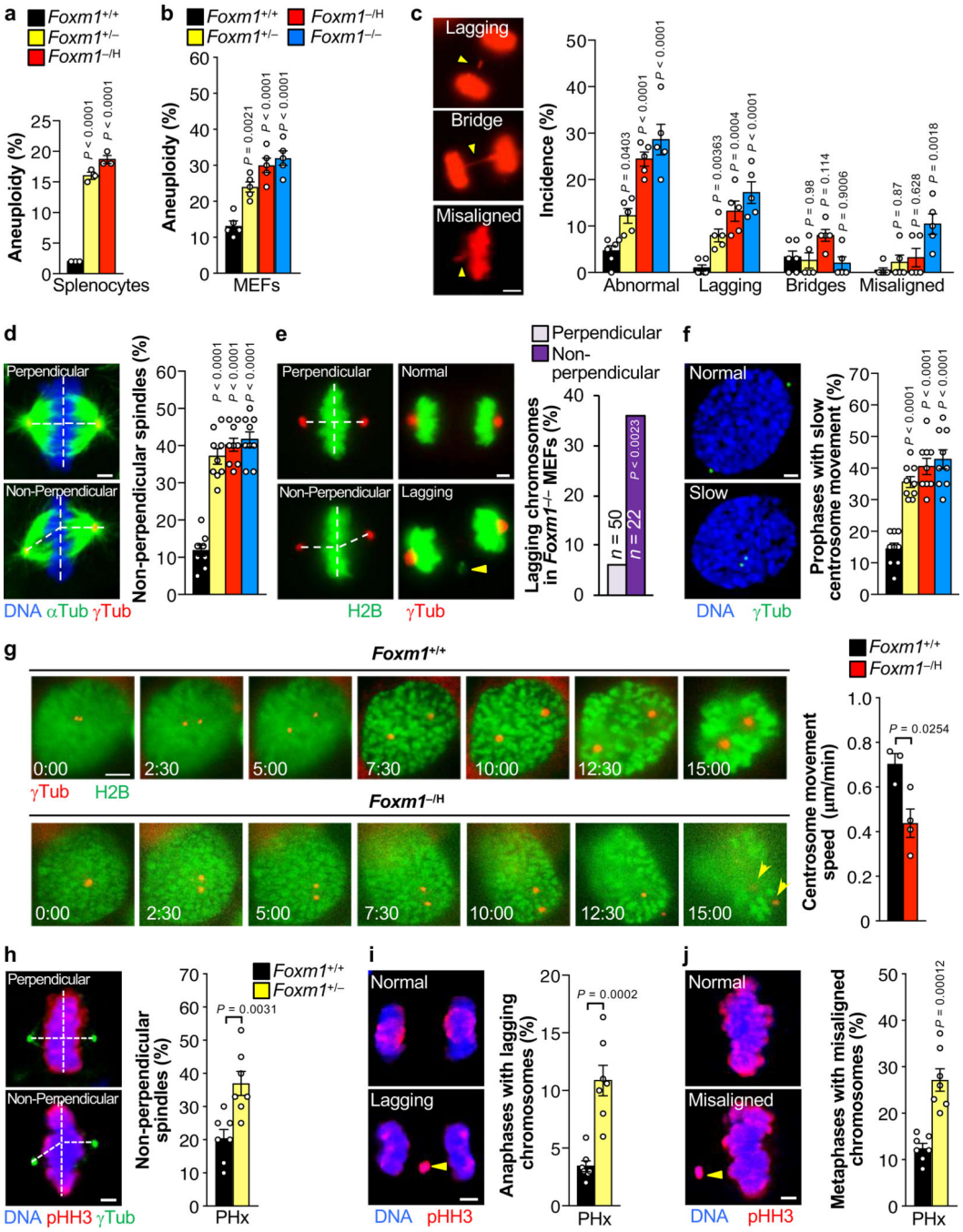

Figure 2. FoxM1 controls centrosome movement and perpendicular spindle assembly.

(a) Chromosome counts on splenocytes from 5-month-old mice (n = 3 mice per group) and **(b)** MEFs (n = 5 independent MEF lines per group) of indicated genotypes. **(c)** Left: Representative images of observed chromosome segregation defect. Right: Chromosome segregation analysis of MEFs expressing H2B-mRFP(n = 6 +/+ 5 +/−, 5 −/H, and 5 −/− MEF lines). **(d)** Left: Images of MEFs in metaphase immunostained with αTubulin and γTubulin. Right: Quantification of cells with non-perpendicular mitotic spindles (n = 9 independent MEF lines per group). **(e)** Left: Images of *Foxm1*$^{-/-}$ MEFs followed

by time-lapse microscopy just before and after anaphase onset. Right: Incidence of lagging chromosomes resulting from metaphases with perpendicular or non-perpendicular spindles (n = 50 perpendicular and 22 non-perpendicular spindles). **(f)** Images of MEFs in prophase immunostained with γTubulin. Right: Quantification of cells with slow centrosome movement (n = 9 independent MEF lines per group). Legend as in **b**. **(g)** Left: Timelapse images of centrosome movement in MEFs expressing H2B-YFP and γTubulin-tdTomato. Time is indicated in min. Right: Speed of centrosome movement (n = 3 +/+ and 4 −/H independent MEF lines) **(h)** Left: Images of metaphases in liver sections of 8-week-old mice, 50–52 h after partial hepatectomy (PHx), immunostained with phospho-histone $H3^{Ser10}$ (pHH3) and γTubulin. Right:Quantification of metaphases with non-perpendicular spindles (n = 7 mice per group). **(i)** Left: Images of a normal anaphase and anaphase with lagging chromosome. Right: Quantification of anaphases with lagging chromosomes as in **h**. **(j)** Left: Images of a normal metaphase and metaphase with misaligned chromosome. Right: Quantification of metaphases with misaligned chromosomes as in **h**. Data in **a-d**, **f-j** represent mean ± s.e.m. Statistics: **a-d**, **f** one-way ANOVA with Tukey's correction; **e**, two-tailed Fisher's exact test; **g-j**, two-tailed unpaired t-test. Scale bar, 5 μm See source file for original data.

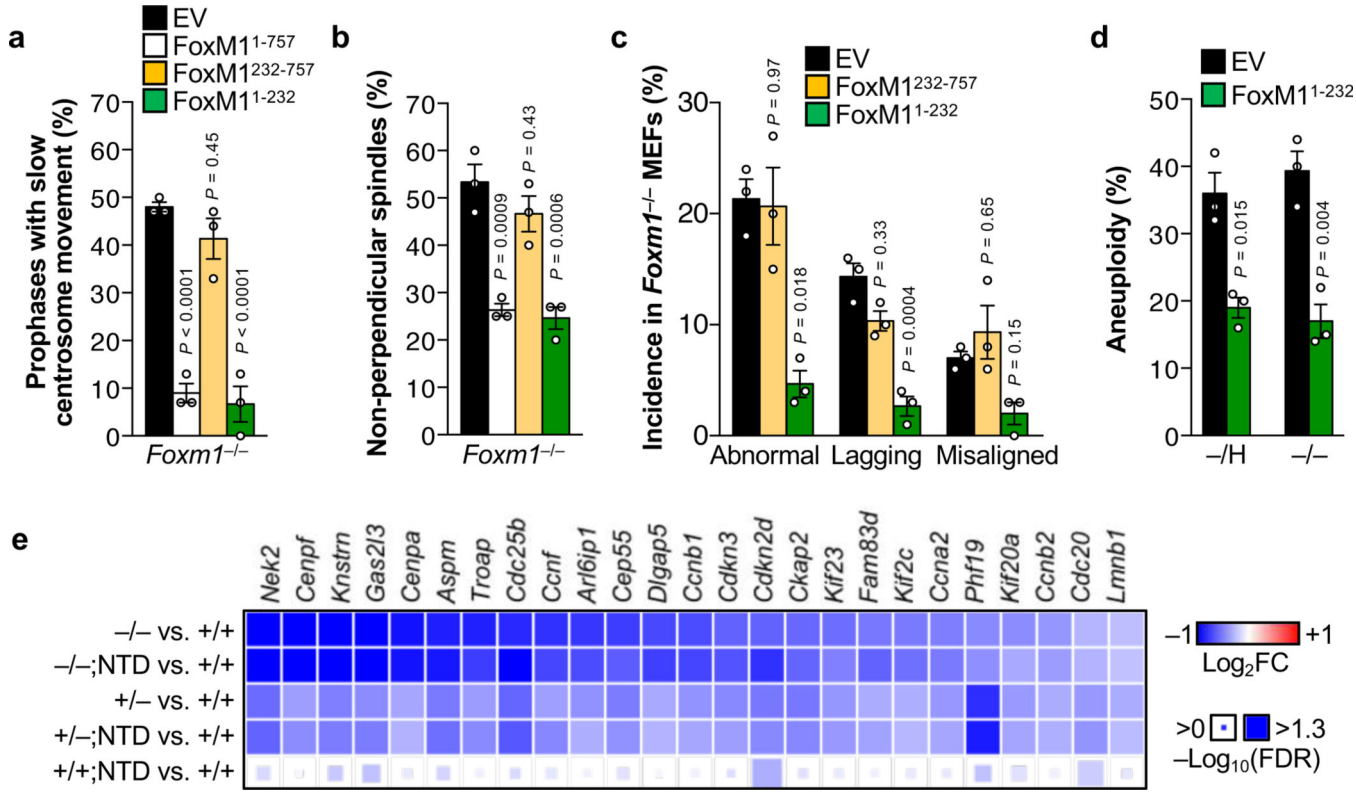

Figure 3. The FoxM1 NTD non-transcriptionally regulates centrosome movement.

(a-c) *Foxm1*$^{-/-}$ MEFs stably expressing indicated cDNA constructs analyzed for incidence of slow centrosome movement in prophase **(a)**, non-perpendicular spindles in metaphase **(b)**, and chromosome segregation errors **(c)**. **(d)** Chromosome counts on *Foxm1*$^{-/H}$ (−/H), *Foxm1*$^{-/-}$ (−/−) MEFs stably expressing the indicated cDNA constructs. **(e)** Heat map showing Log_2 fold change of indicated FoxM1 transcriptional targets in RNA sequencing experiments. Abbreviations: +/+, *Foxm1*$^{+/+}$ MEFs; −/−, *Foxm1*$^{-/-}$ MEFs; −/−;NTD, *Foxm1*$^{-/-}$ MEFs expressing FoxM$^{1–132}$; +/−, *Foxm1*$^{+/-}$ MEFs. We note that none of the changes are significant for +/+;NTD vs +/+ comparison. *n* = 3 independent MEF lines per group for all experiments. Data in **a-d** represent mean ± s.e.m. Statistics: **a-c**, one-way ANOVA with Tukey's correction; **d**, two-tailed paired *t*-test. See source file for original data.

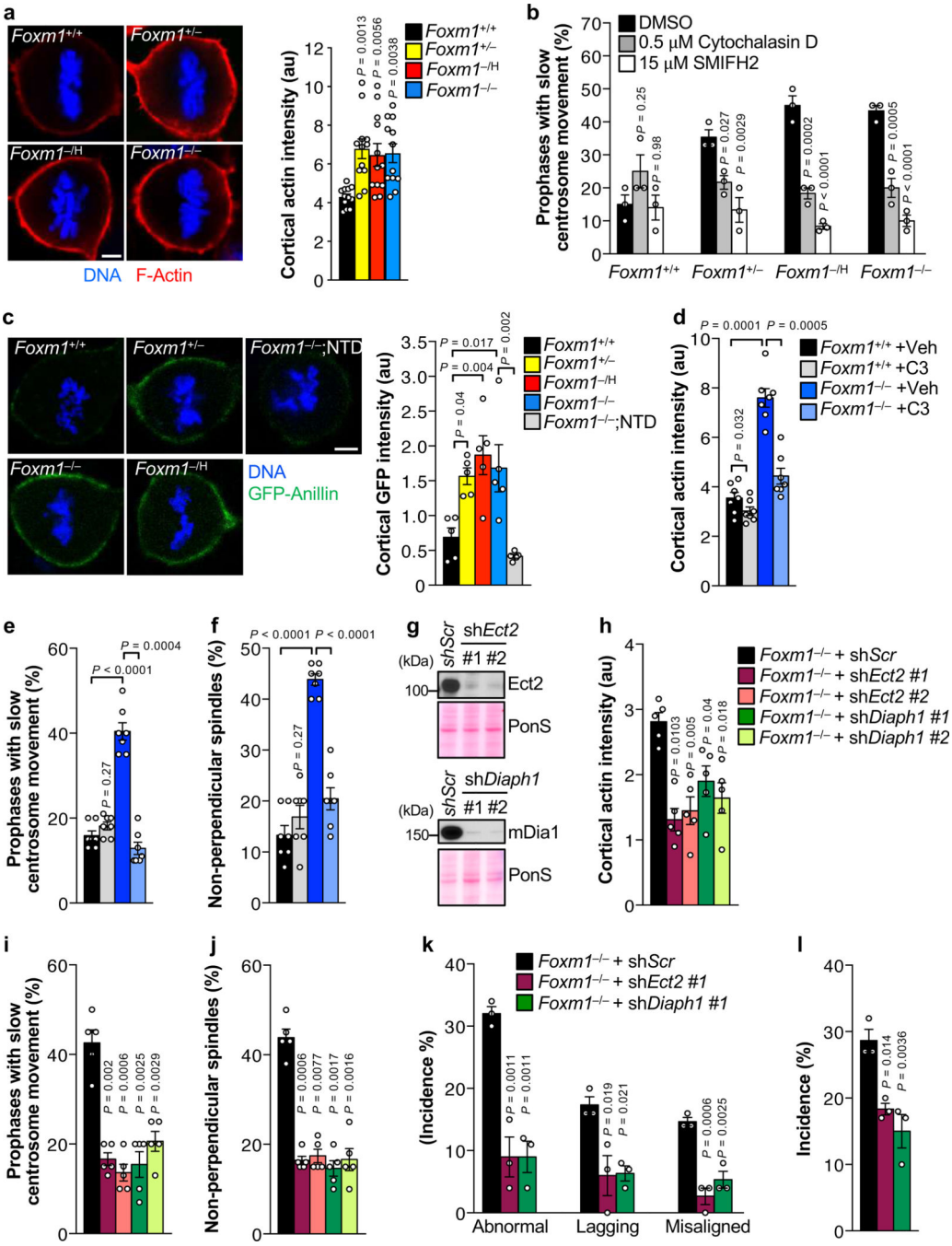

Figure 4. The FoxM1 NTD acts to inhibit cortical actin nucleation

(a) Left: Images of indicated MEFs in metaphase stained with TRITC-Phalloidin. Right: Quantification of mitotic cortical actin intensity of the indicated MEFs (n = 12 independent MEF lines per group). **(b)** Incidence of slow centrosome movement in the indicated prophases treated Cytochalasin D (Cyto D; actin depolymerizer) or SMIFH2 (pan-Formin inhibitor) for 4 h. Significance is denoted for comparison between the DMSO and treatment groups within each genotype (n = 3 independent MEF lines per group). **(c)** Left: Images of the indicated MEFs expressing GFP-anillin (RhoA biosensor). Right: Quantification of

GFP-anillin intensity at the cell cortex in the indicated MEFs (n = 5 independent MEF lines per group). **(d)** Quantification of cortical actin intensity in indicated MEFs treated with vehicle (Veh) or 1.5 μg/ml RhoA inhibitor (C3) for 4 h (n = 7 independent MEF lines per group). **(e)** Incidence of slow prophase centrosome movement and **(f)** Quantification of cells with non-perpendicular spindles in the indicated MEFs as in **d** (n = 7 independent MEF lines per group). **(g)** Western blot analysis of *Foxm1*$^{-/-}$ MEFs stably transduced with the indicated shRNAs. Western blots are representative of 5 independent MEF lines. **(h-l)** *Foxm1*$^{-/-}$ MEFs stably transduced with the indicated shRNAs and then analyzed for cortical actin intensity in metaphase **(h)**, non-perpendicular mitotic spindles **(i)**, slow centrosome movement in prophase, **(j)**, chromosome segregation errors **(k)**, and aneuploid metaphase spreads **(l)**. n = 5 independent MEF lines per group in **h-j** and 3 independent MEF lines per group in **k, l**. Data represent mean ± s.e.m. Statistics: **a-l** one-way ANOVA with Sidak's correction; Scale bar, 5 μm. See source file for original data and uncropped immunoblots.

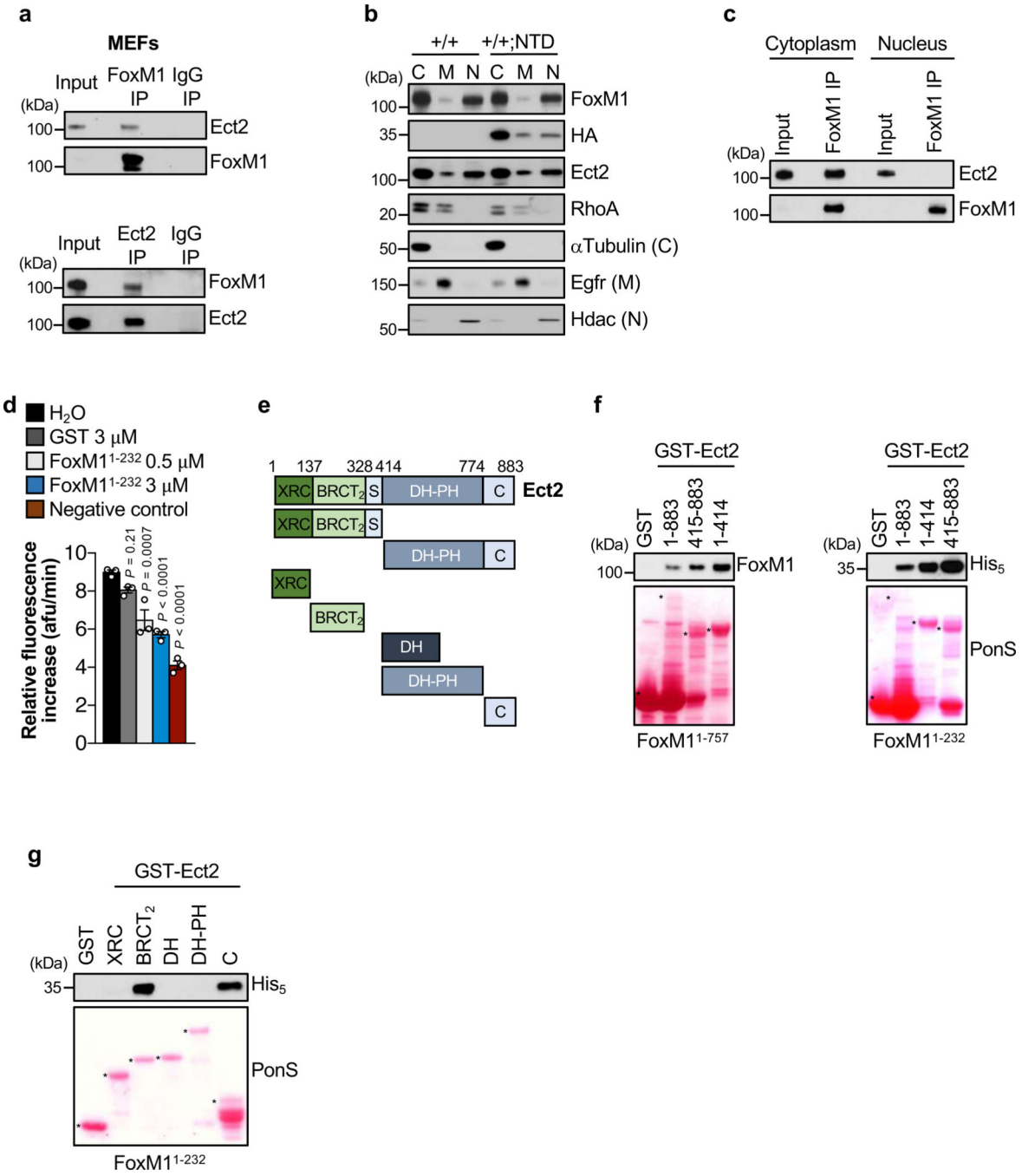

Figure 5. Cytoplasmic FoxM1 binds to and inhibits the GEF activity of Ect2 towards RhoA

(a) Top: FoxM1 immunoprecipitation from whole-cell wildtype MEF extracts. Bottom: Ect2 immunoprecipitation from whole-cell wildtype MEF extracts. **(b)** Western blots of *Foxm1*$^{+/+}$ MEFs (+/+) with and without HA-FoxM1$^{1–232}$ (NTD) subject to subcellular fractionation: C, cytoplasmic fraction; M, membrane fraction; and N, nuclear fraction. **(c)** FoxM1 immunoprecipitation from fractionated wildtype MEF extracts. **(d)** Quantification of nucleotide exchange activity of immunoprecipitated Ect2 towards RhoA in presence of indicated recombinant proteins (n = 3 independent experiments). Negative control,

no immunoprecipitated Ect2. **(e)** Schematic showing Ect2 domains and constructs used for experiments. Numbers indicate amino acid residues. **(f)** *In vitro* binding assay using indicated GST-Ect2 mutants and (left) His-FoxM1$^{1–757}$ or (right) His-FoxM1$^{1–232}$. **(g)** *In vitro* binding assay using indicated GST-Ect2 mutants and His-FoxM1$^{1–232}$. PonS staining shows expression of recombinant GST proteins (marked by asterisks) in **f** and **g**. All western blots are representative of at least 3 independent experiments. Data represent mean ± s.e.m in **d**. Statistics: **d**, one-way ANOVA with Tukey's correction. See source file for original data and uncropped immunoblots.

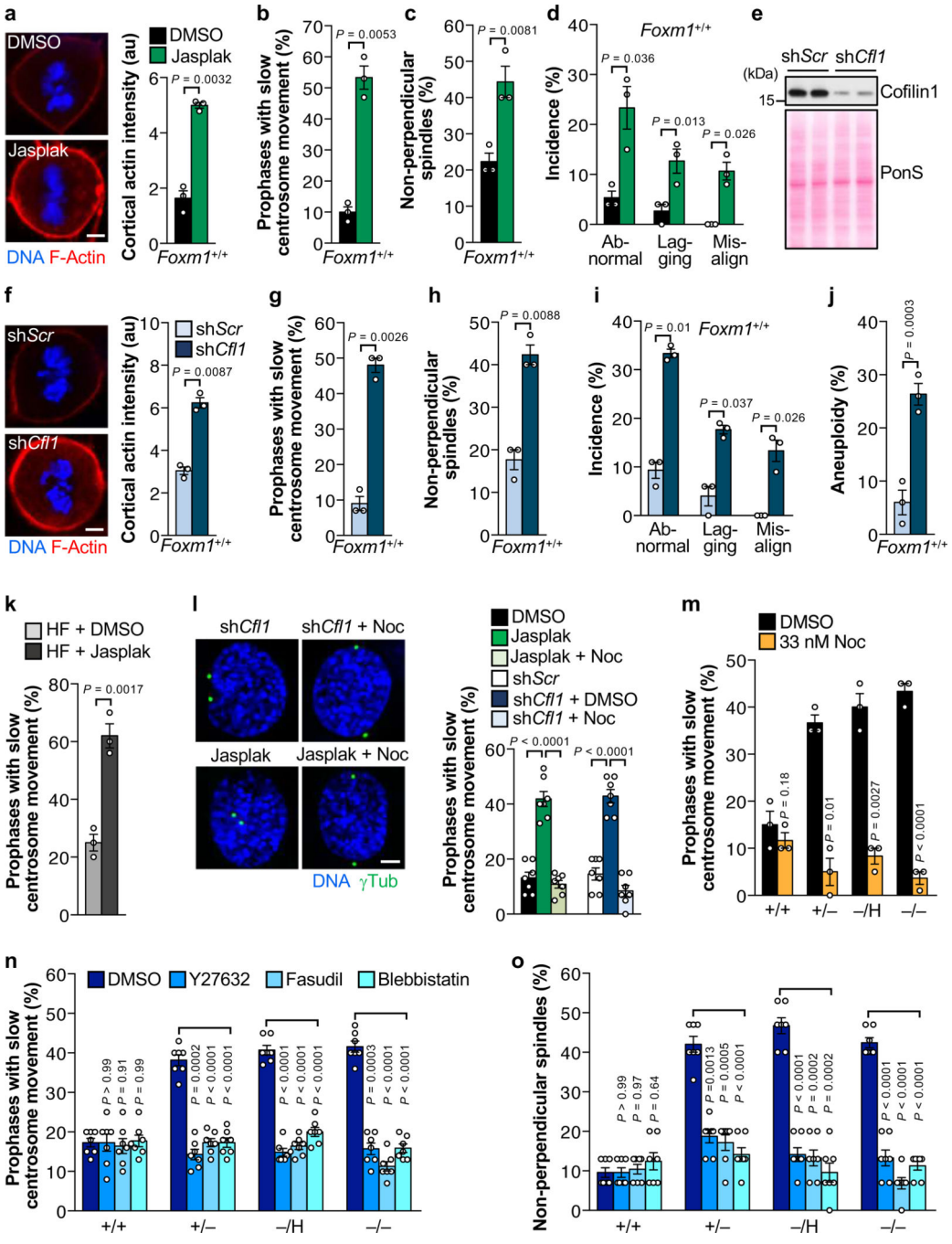

Figure 6. Excessive cortical actin rigidity slows centrosome movement regardless of cause.

(a) Left: Images of wildtype (*Foxm1*$^{+/+}$) MEFs in metaphase cultured in the presence of DMSO or 100 nM Jasplakinolide (Jasplak) for 4 h and stained with TRITC-Phalloidin. Right: Quantification of cortical actin intensity. (*n* = 3 independent wildtype MEF lines per group).**(b-d)** Wildype MEFs cultured in the presence of DMSO or 100 nM Jasplakinolide for 4 h and then analyzed for slow prophase centrosome movement **(b)**, non-perpendicular spindles in metaphase **(c)**, chromosome segregation errors **(d)** (*n* = 3 independent wildtype MEF lines per group). **(e)** Western blot analysis of wildtype MEFs stably transduced

with scramble (*scr*) or *Cfl1* shRNA. Western blot is representative of 3 independent MEF lines per group. **(f)** Left: Images of MEFs stained with TRITC-Phalloidin. Right: Quantification of cortical actin intensity(n = 3 independent MEF lines per group). **(g-j)** Wildtype MEFs stably transduced with scramble (*scr*) or *Cfl1* shRNA analyzed for slow prophase centrosome movement **(g)**, non-perpendicular spindles in metaphase **(h)**, chromosome segregation errors **(i)**, aneuploid metaphase spreads **(j)** (n = 3 independent wildtype MEF lines per group). **(k)** Quantification of prophases with slow centrosome movement in primary HSFs treated with DMSO or 100 nM Jasplakinolide for 4 h (n = 3 independent HSF lines per group). **(l)** Left Top: Images of wildtype MEFs stably transduced with *scr* or *Cfl1* shRNA treated with DMSO or 33 nM nocodazole (Noc) for 4 h to depolymerize astral microtubules. Left Bottom: Images of WT MEFs treated with DMSO or 100 nM Jasplakinolide simultaneously treated with 33 nM nocodazole for 4 h. Right: Quantification of slow prophase centrosome movement in wildtype MEFs treated as indicated (n = 7 independent MEF lines per group). **(m-n)** Quantification of slow prophase centrosome movement in the indicated MEFs treated with the indicated compounds or corresponding vehicle indicated for 4 h (n = 3 and n = 7 independent MEF lines per group, in **m** and **n**, respectively). **(o)** Incidence of non-perpendicular metaphase spindles in MEFs of the indicated genotypes and treated with the indicated compounds or vehicle (n = 7 independent MEF lines per group). See methods for drug concentrations. Data represent mean ± s.e.m. Statistics: **a-d, f-k, m** two-tailed paired *t*-test; **l, n, o**, one-way ANOVA with Tukey's correction. Scale bars, 5 μm. See source file for original data and uncropped immunoblots.

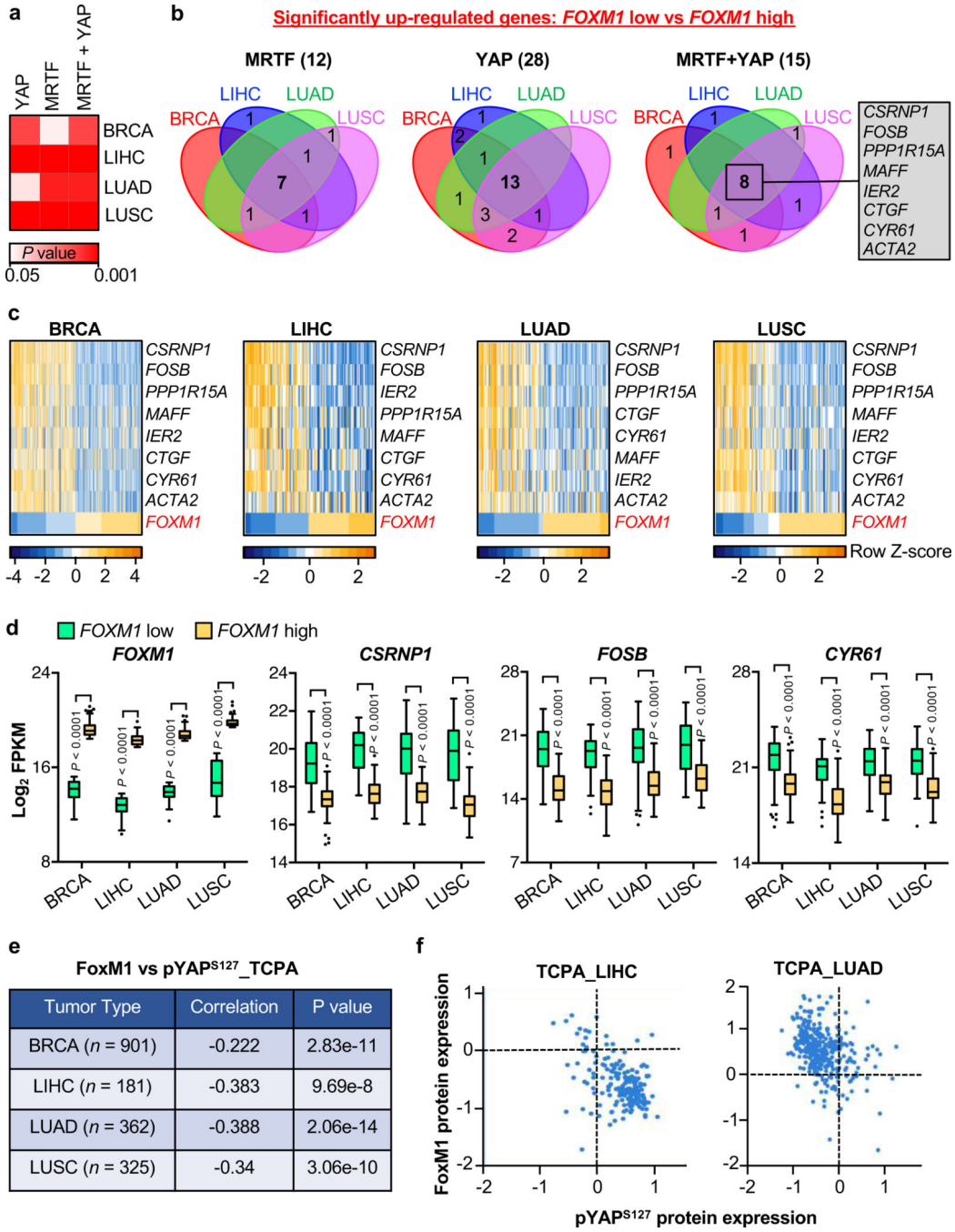

Tumor Type	Correlation	P value
BRCA (*n* = 901)	-0.222	2.83e-11
LIHC (*n* = 181)	-0.383	9.69e-8
LUAD (*n* = 362)	-0.388	2.06e-14
LUSC (*n* = 325)	-0.34	3.06e-10

Figure 7. Low *FOXM1* expression correlates with high RhoA activity in several human cancer types.

(a) Overrepresentation of gene expression signatures driven by YAP and/or MRTF-A in the indicated *FOXM1* groups and tumor types. LogfcMLE −1 was used as cut-off. Significance derived by one-tailed Fisher's exact test. **(b)** Venn diagrams showing the number of significantly upregulated genes for the indicated signatures, in *FOXM1* groups, and tumor types. Parentheses indicate the total number of genes in each signature. MRTF-A + YAP commonly upregulated genes across the four indicated tumor types are indicated.

See Supplementary Table 4 for gene list. **(c)** Heat maps showing expression levels of the commonly upregulated genes (listed in **b**) in human tumors with low *FOXM1* of the indicated type. **(d)** Expression of select genes between *FOXM1* low and *FOXM1* high groups. Box-whisker plots generated according to Tukey's method where box represents the median (central line), upper (75^{th}) and lower quartiles (25^{th}) and whiskers represent 1.5x interquartile range (IQR). Outliers (75^{th} percentile +1.5x IQR or 25^{th} percentile −1.5x IQR) are shown as individual data points. See number of patients in each group below. Significance derived by two-tailed unpaired *t*-test with Welch's correction. **(e)** Correlation analysis between FOXM1 protein levels and inhibitory Ser127 phosphorylation on YAP from the cancer proteome atlas (TCPA) in indicated tumor types. **(f)** Scatter plots displaying protein expression of FOXM1 and phosphorylated YAP^{Ser127} from patients of indicated tumor types obtained from TCPA. BRCA; Breast cancer (n = 182 *FOXM1* low group and n = 184 *FOXM1* high group), LIHC; Liver hepatocellular carcinoma (n = 63 *FOXM1* low group and n = 65 *FOXM1* high group), LUAD; Lung adenocarcinoma (n = 87 *FOXM1* low group and n = 89 *FOXM1* high group), LUSC; Lung squamous cell carcinoma (n = 82 *FOXM1* low group and n = 84 *FOXM1* high group). See source file for original data.

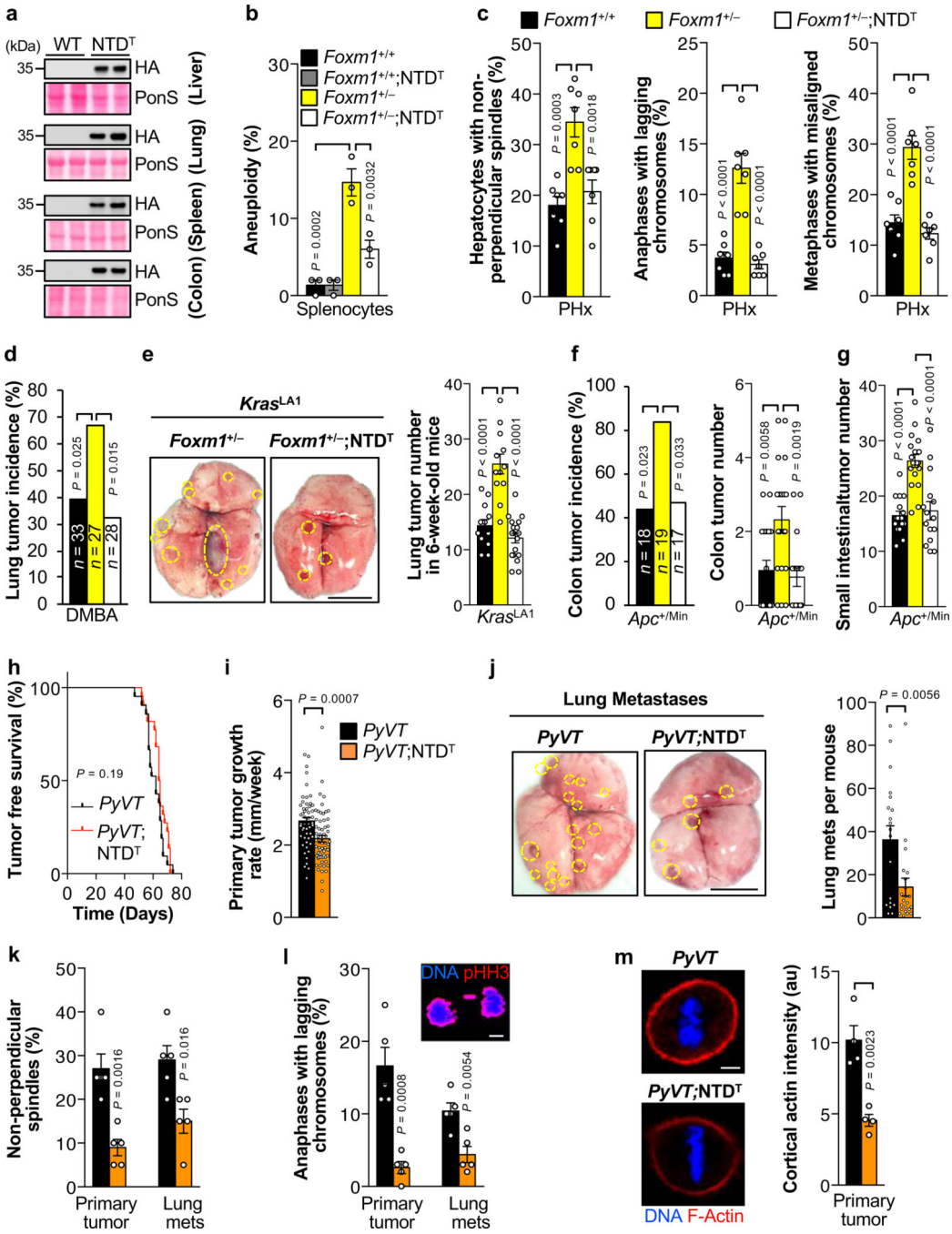

Figure 8. Correction of cortical actin hypernucleation by NTD overexpression inhibits tumorigenesis.

(a) Western blot analysis showing expression of transgenic HA-FoxM1$^{1–232}$ (NTD^{T}) in different mouse tissues. PonceauS (PonS) staining of blotted proteins served as loading control. Western blots are representative of at least 4 independent mice per genotype. **(b)** Chromosome counts performed on splenocytes from 5-month-old mice (n = 3 mice per group). **(c)** Quantification of metaphases with non-perpendicular spindles, anaphases with lagging chromosomes and metaphases with misaligned chromosomes in liver sections of

8-week-old mice of the indicated genotypes, 50–52 h after partial hepatectomy (PHx) (n = 7 mice per group). **(d)** Lung tumor incidence in 4-month-old mice after DMBA treatment (n = 27–33 mice per group). **(e)** Left: Images of lung tumors of the indicated mice on $Kras^{LA1}$ background. Right: Lung tumor multiplicity of 6-week-old mice of the indicated genotypes (see **c** for legend) on $Kras^{LA1}$ background (n = 12 +/+, 12 +/− and 18 +/−; NTD^{T} mice). **(f-g)** Incidence and multiplicity of colon tumors **(f)** and multiplicity of small intestinal tumors **(g)** of 90-day-old mice of the indicated genotypes on a $Apc^{+/Min}$ background (n = 18 +/+, 19 +/−, and 17 +/−;NTD^{T} mice). **(h)** Tumor-free survival of MMTV-*PyVT* mice with and without NTD^{T} (n = 21 *PyVT* mice and 22 *PyVT*; NTD^{T} mice). **(i)** Mean tumor growth rate of primary mammary tumors (n = 51 *PyVT* tumors and 61 *PyVT*; NTD^{T} tumors). **(j)** Left: Images of lung metastases 6 weeks after the first tumor was detected by palpation. Right: Number of metastatic (mets) lung tumors (n = 19 *PyVT* mice and 22 *PyVT*; NTD^{T} mice). **(k)** Quantification of metaphases with non-perpendicular spindles in tumor-derived epithelial cells (n = 5 individual lines per group). **(l)** Incidence of lagging chromosomes in tumor-derived epithelial cells. Image shows an anaphase with lagging chromosome (n = 5 individual lines per group). **(m)** Left: Images of epithelial cells from mammary tumors stained with TRITC-Phalloidin. Right: Quantification of cortical intensity in epithelial cells derived from the primary mammary tumor (n = 4 individual lines per group). Data represent mean ± s.e.m. Statistics: **b, c,** and **e, f, g** one-way ANOVA with Tukey's correction; **d, f (incidence)**, two-tailed Fisher's exact test; **h**, log-rank Mantel-Cox test; and **i-m**, two-tailed unpaired t-test. Scale bars, **e**, **j** 5 mm and **l**, **m** 5 μm. See source file for original data and uncropped immunoblots.